Interaction of (3-Aminopropyl)triethoxysilane With Late Ar-N 2 Afterglow: Application to Nanoparticles Synthesis

Magamou Gueye, Thomas Gries, Cédric Noel, Sylvie Migot-Choux, Simon Bulou, Elodie Lecoq, Patrick Choquet, Thierry Belmonte

▶ To cite this version:

Magamou Gueye, Thomas Gries, Cédric Noel, Sylvie Migot-Choux, Simon Bulou, et al.. Interaction of (3-Aminopropyl)triethoxysilane With Late Ar-N 2 Afterglow: Application to Nanoparticles Synthesis. Plasma Processes and Polymers, 2016, 13 (7), pp.698-710. 10.1002/ppap.201500201 . hal-02113596

HAL Id: hal-02113596
https://hal.science/hal-02113596v1

Submitted on 14 May 2019

Interaction of (3–Aminopropyl)triethoxysilane with late Ar-N_2 afterglow: Application to nanoparticles synthesis

M. Gueye[1,2], T. Gries[1,2], C. Noël[1,2], S. Migot-Choux[1,2], S. Bulou[3], E. Lecoq[3], P. Choquet[3], T. Belmonte[1,2]

[1] Université de Lorraine, Institut Jean Lamour, UMR CNRS 7198, NANCY, F-54011, France

[2] CNRS, Institut Jean Lamour, UMR CNRS 7198, NANCY, F-54011, France

[3] Luxembourg Institute of Science and Technology, MRT Department, 5 avenue des Hauts-Fourneaux, L-4362 Esch/Alzette

* corresponding author. Email: thierry.belmonte@univ-lorraine.fr

Keywords: (3–Aminopropyl)triethoxysilane, nitrogen afterglow, plasma polymer, nanoparticles.

ABSTRACT

From results of *in situ* FTIR absorption and optical emission spectroscopy, the interaction of (3–Aminopropyl)triethoxysilane (APTES) with late Ar-N_2 afterglow is shown to occur mainly with N atoms, $N_2(A)$ states having a negligible role. The $N_2(X,v)$ states might contribute to the dissociation process if they are sufficiently excited, but this contribution is expected to be limited. N atoms react preferentially with carbon from CH_x groups in the precursor, leading to the synthesis of CN bonds. No production of NH radical is observed, demonstrating the lack of direct reaction between active nitrogen species and hydrogen from the APTES. Excited CN radicals are produced via either $\mathrm{C + N + M \rightarrow CN^{*} + M}$ or $\mathrm{N + CH \rightarrow CN^{*} + H}$. CO molecules are produced from oxygen and carbon available within the precursor, enabling the synthesis of siloxane groups. The $-NH_2$ group is not affected by the afterglow but it is not found in the nanoparticles collected from the gas phase. One of the C–C bonds of the propylamine group in the APTES is likely broken, leaving a non-reactive gaseous compound which is removed by the gas flux. These nanoparticles present a non-negligible content in nitrogen under the form of secondary amides due to reactions with active nitrogen. They are amorphous and react efficiently with water and carbon dioxide from the air to likely produce a salt.

GRAPHICAL ABSTRACT

The synthesis of nanoparticles by interaction between a late Ar-N_2 afterglow (3–Aminopropyl)triethoxysilane, a organosilicon compound containing one amine functional group, is shown to lead to an amorphous material containing amide functional groups produced by nitrogen atoms of the afterglow.

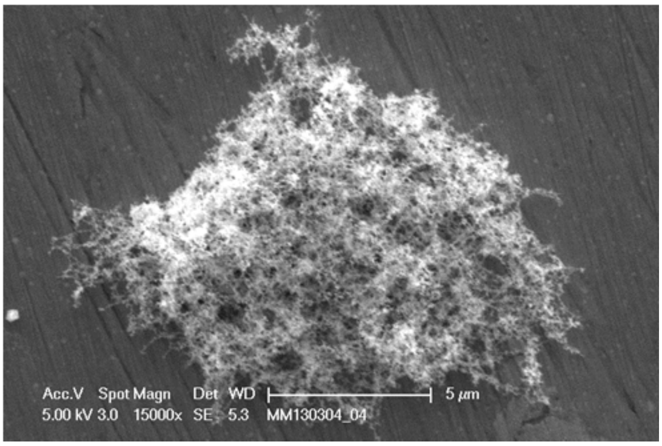

1. INTRODUCTION

Advanced bio-devices such as cell microarrays, biosensors and advanced drug delivery systems need investigation of a number of new features of biological systems. These devices are commonly based on patterned and switchable properties which are needed to effectively manipulate biomolecules both spatially and temporally [1-3]. More specifically, patterned surfaces functionalized by primary amines ($–NH_2$) are sought to assist cell or enzyme attachment [4, 5]. Several precursors containing a primary amine as functional group can be chosen to modify surface reactivity. (3–Aminopropyl)triethoxysilane (APTES, $(C_2H_5O)_3–Si–(CH_2)_3–NH_2$) is a colourless transparent liquid. It is usually preferred to allylamine when silanization is needed [5]. From its vapour, deposition of a thin film containing primary amines can be achieved. APTES is commonly used as a coupling agent in composites, coatings, adhesive joints or glass fibres for covalently binding proteins to inorganic surfaces [6].

The presence in the coating of primary amines is usually difficult to achieve. The deposition of APTES is complex, often resulting in multilayer deposition and irregular surface morphology [7-9]. After deposition, APTES can undergo further chemical changes (curing). When it is only partially cured, APTES presents a complicated structure [10]. Better understanding the chemical pathways leading to deposition from APTES is then essential to improve the growth of amine-containing thin films. Direct plasma-assisted processes should be avoided because electron collisions alter the amine function. The only way to preserve it is to work in pulsed mode or in remote conditions, *i.e.* in afterglow. Electron collisions are either limited or suppressed and a soft treatment is possible, leading ideally to radical synthesis by abstraction of H atoms for instance while keeping as much as possible the integrity of the molecule. As-formed radicals can undergo subsequent crosslinking, either in the gas phase or on a surface, to form a plasma-polymer containing intact NH_2 groups.

In this work, we study the decomposition of APTES in a Lewis-Rayleigh Ar–N_2 afterglow. A special attention is also paid to the synthesis of APTES-like nanoparticles. Indeed, nanomaterials with precise biological functions have considerable potential for use in biomedical applications [11]. Fourier transform infrared (FTIR) spectroscopy and optical emission spectroscopy are used as *in situ* investigation methods of the gas phase. Although several publications report the use of APTES in Plasma-Enhanced Chemical Vapour Deposition processes [12–17], no basic studies dealing with APTES decomposition in the gas phase have been undertaken to date.

2. EXPERIMENTAL METHOD

The experimental set-up is presented in figure 1. A surface wave-excited plasma is created in a 5 mm inner diameter cylindrical fused silica tube exposed to 2.45 GHz microwaves by means of a surfatron wave launcher. The delivered microwave power is kept constant at 100 W. Pressure was measured in points A and E (see figure 1). All the treatments are carried at 2026 Pa measured in point A – the pressure in point E being 2533 Pa in an Ar–8.7vol.% N_2 mixture, flowing at 1150 sccm. 15 cm downstream, the plasma reaches a 1.2 meter long fused silica tube (16 mm inner diameter) crossed by the infrared beam. The vapour above liquid APTES (99.0% purity, purchased from Sigma Aldrich and used without further treatment) contained in a temperature-controlled bubbler system is dragged away by an argon flow (30 sccm) blown into the reactor via a second 5 mm inner diameter cylindrical fused silica tube (point B in figure 1). The partial pressure of APTES was determined using Antoine’s formula from experimental data obtained by probing the FTIR absorption signal of pure APTES evaporated at temperatures ranging from 300 K to 390 K:

$$Log_{10}\left(\frac{P_s}{P_{ref}}\right)=1.6 - \left(\frac{2384.4}{T(\mathrm{K})+300}\right) \tag{1}$$

where P_s is the vapour pressure (in Pa), P_{ref} the standard pressure (101325 Pa) and T the temperature (K). Then, at 300 K, P_s / P_{ref} = 4.23×10^{-3} and the APTES flow rate was 0.13 sccm in the Ar-N_2 afterglow.

For optical emission spectroscopy (OES), afterglow light was collected by an optical fibre connected to 550 mm focal length monochromator (Jobin–Yvon TRIAX 550) equipped with a 100 grooves mm^{-1} grating for survey spectra in the range [250–900 nm] and a 1,800 grooves mm^{-1} grating to record specific transitions with high spectral resolution. The spectrometer was coupled with a HORIBA Jobin–Yvon i-Spectrum Two iCCD detector. Each measurement was averaged over 20 spectra.

Time-resolved OES measurements were performed at 1520 Pa to determine the gas velocity after the mixing point between the afterglow and the Ar-APTES mixture. Pressure had to be lowered a bit to enable self-ignition of the discharge in pulse mode. The discharge was pulsed with a period of 100 ms, the duty cycle being 60% (no Ar-APTES mixture was introduced in these experiments). The time laps between plasma ignition and the intensity rise of the N_2 ($B^3\Pi_g$, v'=11 → $A^3\Sigma_u^+$, v''=7) transition at 580.43 nm, *i.e.* the time required for the gas to flow from the plasma gap to the optical fibre, was recorded for different positions of the optical fibre located downstream point B used here as reference (see **supplemental material 1a**). The average velocity in the afterglow tube is given by plotting the distance to B as a function of time laps (see **supplemental material 1b**). A straight line is effectively found and its slope gives the gas velocity. A value of 7.6 ± 0.1 m s^{-1} was found. The gas temperature being 300 K, the theoretical velocity at 1520 Pa is estimated to 6.98 m s^{-1}, which is in good agreement. Then, the gas velocity beyond point B is estimated to be 5.7 m s^{-1} at 2026 Pa considering the addition of the Ar-APTES mixture and a gas temperature close to room temperature.

FTIR spectroscopy was performed with a commercial Agilent FTIR 680 spectrometer. The infrared beam leaving the spectrometer goes through lenses and collimators to get a parallel beam (1.6 mm in diameter). This optical arrangement decreases the intensity of the exiting beam by one order of magnitude typically. The infrared beam is next sent through a KBr window in the afterglow (single pass) and detected by a remote liquid-nitrogen cooled mercury-cadmium-telluride (MCT) detector which is protected from the afterglow by another KBr window. To minimize the influence of water and CO_2, the infrared path outside the afterglow was continuously flushed by dry air. Absorption spectra are recorded in the range [500–4000 cm^{-1}] with a spectral resolution of 2 cm^{-1}. Reference spectra (*i.e.* either without gas and plasma or with gas but without plasma) were acquired before each acquisition to determine the absorption spectra in afterglow conditions. Each measurement is averaged over 100 scans in continuous mode to improve the signal-to-noise ratio.

Nanoparticles were collected on an aluminium substrate located just before the pumping unit. Transmission electron microscopy (TEM) investigation was performed on as-grown nanoparticles with a JEOL ARM 200F – Cold FEG TEM/STEM running at 200 kV (point resolution 0.19 nm) fitted with a GIF Quantum ER. Scanning Electron Microscopy (SEM) was made with a Philips XL 30. FTIR measurements on nanoparticles were performed with a commercial Agilent FTIR Cary 610 spectrometer in attenuated total reflection (ATR) mode. Spectra were acquired in the range [500–4000 cm^{-1}] with a spectral resolution of 2 cm^{-1}.

X-ray photoelectron spectroscopy (XPS) measurements are performed with a Thermo VG Microlab350 spectrometer using a non-monochromated Al Kα and Mg Kα dual anode as X-ray source operated at 300 W and a Spherical Sector Analyser. Survey spectra to identify elements on the surface were recorded in steps of 1 eV at a 100 eV pass energy. High resolution spectra of separate photoelectron lines (C 1s, O 1s, Si 2p and N 1s) were taken by steps of 0.05 eV at a constant pass energy of 20 eV. The normal operation pressure was 5×10^{-9} mbar. The photoelectron take-off angle (TOA) was normal to the surface of the samples. The sample surface covered by the analysis is 2×5 mm^2. Spectra processing (atomic concentrations, curve fitting, etc.) was done after the removal of a Shirley type background with the CasaXPS software. Samples are introduced in the spectrometer readily after plasma treatment in order to limit contamination from ambient air storage and directly analysed.

3. RESULTS AND DISCUSSION

3.1. Optical emission spectroscopy

The Ar–N_2 afterglow is characterized by transitions of the N_2 first positive system N_2 ($B^3\Pi_g$, $v' \rightarrow A^3\Sigma_u^+$, v'') with strong intensities (figure 2 and table 1). The (v'=11, v''=7) is the most intense line, which is a well-known feature of late Ar–N_2 afterglows. Transitions of the second positive system N_2 ($C^3\Pi_u$, $v' \rightarrow B^3\Pi_g$, v'') are also present. Moderate transitions of the NOβ system NO ($B^2\Pi$, $v' \rightarrow X^2\Pi$, v'') and weak transitions of the NOγ system NO ($A^2\Sigma^+$, $v' \rightarrow X^2\Pi$, v'') are observed, likely because of weak leak flows in the reactor.

When an extra flow of Ar–APTES is added to the Ar–N_2 afterglow (point B in figure 1), new transitions are observed. One finds intense lines of the CN violet system CN ($B^2\Sigma^+$, $v' \rightarrow X^2\Sigma^+$, v''), especially $\Delta v = -1, 0, +1$ transitions. Weak lines of the CN red system CN ($A^2\Pi$, $v' \rightarrow X^2\Sigma^+$, v'') are also clearly observed, especially those belonging to $\Delta v = -3, -4, -5$ and -6 transitions. The CH 4300Å system CH ($A^2\Delta_g$, $v' \rightarrow X^2\Pi_u$, v'') is characterized mainly by its (0,0) band which is the only one to appear, another feature of active nitrogen when a hydrocarbon is introduced [18].

NO-titration was performed following the method described in ref. [19]. An Ar–1.4vol.%NO mixture was introduced instead of the Ar–APTES mixture to determine the concentration of nitrogen atoms at the mixing point with the Ar–N_2 afterglow. This method leads to $[N] = 2.8 \pm 0.8 \times 10^{15}$ cm^{-3}. Thanks to this value, the absolute concentrations of all emitting species, provided they are intense enough, could be determined with an accuracy of about 30%. Indeed, using the following transition at 580.43 nm which is the most intense of the spectrum:

$$N_2(B,v'=11) \rightarrow N_2(A, v''=7) + h\nu \qquad \text{(a)}$$

One finds:

$$I_{580} = \alpha K_{580} \frac{\nu_a^{11-7}}{\lambda_{580}} \left[N_2(B,11)\right] \qquad (1)$$

where α is a unknown calibration factor, K_{580} is a known constant taking into account the spectral response at the considered wavelength λ_{580}. ν_a^{11-7} = 7.8×10^4 s^{-1} [20] is the de-excitation frequency of the observed transition. The absolute concentration of $N_2(B,v'=11)$ states can be related to the nitrogen atom concentration by considering the following set of reactions [19]:

$$N\,(^4S) + N\,(^4S) + (Ar \text{ or } N_2) \rightarrow N_2(B,v'=11) + (Ar \text{ or } N_2) \qquad \text{(b)}$$

$$N_2(B,v'=11) + (Ar \text{ or } N_2) \rightarrow \text{by-products} \qquad \text{(c)}$$

$$N_2(B,v'=11) \rightarrow N_2(A, v'') + h\nu \qquad \text{(d)}$$

with $k_b^{N_2} = 4.4\times10^{-34}$ cm^6 s^{-1} at 300 K [20] and $k_b^{Ar} = 4.0\times10^{-34}$ cm^6 s^{-1} [21] for the production of the level v'=11 only. $k_c^{N_2}$ =3.0×10^{-11} cm^3 s^{-1} [22] and k_c^{Ar} = 3.0×10^{-13} cm^3 s^{-1} [23], here again for the level v'=11 only. $\nu_d^{11-v''}$ = 2.0×10^5 s^{-1} [20]. Then, applying the quasi-steady state approximation, one finds:

$$\left[N_2(B,v'=11)\right] = \frac{k_b^{N_2}[N]^2[N_2] + k_b^{Ar}[N]^2[Ar]}{k_c^{N_2}[N_2] + k_c^{Ar}[Ar] + \nu_d^{11-v''}} \qquad (2)$$

This gives, in the present conditions: $[N_2(B,v'=11)]$ = $10\pm3.0\times10^8$ cm^{-3}, a value which was used to determine the unknown α in Eq.(1).

The absolute concentrations of all identified species were determined with and without APTES (see **supplemental material 2**). The vibrational distribution of $N_2(B)$ is very close to those commonly found in late Ar-N_2 afterglow [19].

The method described in reference [20] was used to determine $N_2(A)$ concentration knowing $N_2(C,1)$ concentration. This method gives a rough estimate of $N_2(A)$ concentration (with a factor of 2, typically), but the spatial evolution of these species is expected to be accurate. This method is then very useful to estimate the rates of the main processes in which $N_2(A)$ is involved. The set of reactions to consider is:

$$N_2(A) + N_2(A) \rightarrow N_2(C,v'=1) + N_2 \tag{e}$$

$$N_2(C,v'=1) + (N_2, Ar) \rightarrow \text{by-products} \tag{f}$$

$$N_2(C,v'=1) \rightarrow N_2(B,v'') + h\nu \tag{g}$$

with $k_e^{v'=1} = 4.1\times10^{-11}$ cm^3 s^{-1}, $k_f^{N_2,v'=1} = 3.0\times10^{-11}$ cm^3 s^{-1} and $\nu_g^{1-v''} = 2.7\times10^{7}$ s^{-1} [20]. After Setser *et al.* [24], $k_f^{Ar} < 3.3\times10^{-12}$ cm^3 s^{-1} for any vibrational state. This value is is also found to be weak by Sulakshin who gives: $k_f^{Ar} < 3.0\times10^{-13}$ cm^3 s^{-1} [25]. Then, the quasi-steady state approximation leads to:

$$[N_2(C,1)] = \frac{k_e^{v'=1}[N_2(A)]^2}{k_f^{Ar,v'=1}[Ar] + k_f^{N_2,v'=1}[N_2] + \nu_g^{1-v''}} \approx \frac{k_e^{v'=1}[N_2(A)]^2}{k_f^{N_2,v'=1}[N_2] + \nu_g^{1-v''}} \tag{3}$$

The concentration of $N_2(C,1)$ is determined from the intensity of the transition of the second positive system at 315.93 nm which arises from this state. It gives: $[N_2(A)] = 1.5\pm0.5\times10^{12}$ cm^{-3}.

3.2. Time evolutions

By knowing the concentrations of N and $N_2(A)$, it is possible to determine their spatial (from point B downwards) and thus their time evolutions (here the discharge is run in the continuous mode) with and without APTES. Results are given in figure 3. Without APTES, nitrogen atoms are essentially lost by the following processes:

$$\mathrm{N}\left({}^4S\right)+\mathrm{N}\left({}^4S\right)+(\mathrm{N}_2 \text{ or Ar}) \rightarrow \mathrm{N}_2(B,v')+(\mathrm{N}_2 \text{ or Ar}) \tag{h}$$

$$\mathrm{N}\left({}^4S\right)+\text{wall} \rightarrow \frac{1}{2}\mathrm{N}_2(X)+\text{wall} \tag{i}$$

with $k_h^{N_2}=8.27\times10^{-34}\exp\left(500/T_g\right)$ cm^6 s^{-1}, *i.e.* 4.4×10^{-33} cm^6 s^{-1} at 300 K [26] and $k_h^{Ar}=(2/6.5)\times k_h^{N_2}$ [19], *i.e.* 1.35×10^{-33} cm^6 s^{-1} at 300 K. The rate constant of process (i) is related to the loss probability γ of N atoms at the wall through:

$$k_i=\frac{\gamma v_{th}}{2R} \tag{4}$$

where R is the tube radius and v_{th} the thermal velocity of N atoms: $v_{th}=\sqrt{8k_BT_g/\pi M}$, where k_B is the Boltzmann constant, T_g, the gas temperature and M the atomic weight of the gas mixture. Then, the loss of nitrogen atoms reads:

$$\frac{d[N]}{dt}=-2k_h^{N_2}[N]^2[N_2]-2k_h^{Ar}[N]^2[Ar]-k_i[N] \tag{5}$$

which, after integration, gives:

$$[N]=\frac{[N]_0}{\exp(\alpha t)-\beta[N]_0(1-\exp(\alpha t))} \tag{6}$$

with $\alpha=k_i$ and $\beta=\left(2k_h^{N_2}[N_2]+2k_h^{Ar}[Ar]\right)/\alpha$.

When APTES is introduced, nitrogen atoms are assumed to be consumed, not only by the aforementioned processes, but also by the following additional process:

$$\mathrm{N}\left({}^4S\right)+\text{APTES} \rightarrow \text{products} \tag{j}$$

The validity of this assumption will be discussed later. The corresponding time evolution is still given by equation (6), but this time with $\alpha=k_i+k_j[\text{APTES}]$.

Fitting the time evolutions without and with APTES gives access to γ and k_j respectively. One finds: $\gamma=2.5\pm0.5\times10^{-5}$ and $k_j=1.8\pm0.6\times10^{-13}$ cm^3 s^{-1}. The loss probability of nitrogen atoms at the walls is among commonly reported values. The value of the rate constant k_j is not unlikely but its meaning is unclear, as discussed hereafter.

The behaviour of $N_2(A)$ also changes in the presence of APTES. The time evolution of $N_2(A)$ in late afterglow is, to a first approximation, ruled by the following loss processes [27, 28]:

$$N_2(A) + N_2(X, 5 \le v \le 14) \to N_2(B) + N_2 \tag{k}$$

$$N_2(A) + N(^4S) \to N_2(X, 6 \le v \le 9) + N(^2P) \tag{l}$$

$$N_2(A) + \mathrm{w}\mathit{all} \to N_2(X, v) + \mathrm{w}\mathit{all} \tag{m}$$

together with the following gain process:

$$N_2(X, v \ge 10) + N(^2P) \to N_2(A) + N(^4S) \tag{n}$$

with $k_k = 2.0 \times 10^{-11}$ cm^3 s^{-1} [26], $k_l = 4.0 \times 10^{-11}$ cm^3 s^{-1} [19] and $k_m = 320$ s^{-1} at 300 K using the data by Piper [29]. $k_n \approx 4.0 \times 10^{-11}$ cm^3 s^{-1} [27]. Processes (k) and (m) weakly contribute to $N_2(A)$ losses. On the other hand, process (l) is very fast but counterbalanced by process (n) which is, somehow, the corresponding reverse process [27].

We need an estimate of the concentration of $N(^2P)$. The steady-state approximation used in reference [27] is applied here to find $[N(^2P)] \approx \frac{k_m[N][N_2(A)]}{k_n[N_2(X, v \ge 10)]}$. This gives $[N(^2P)] \approx \frac{k_m[N][N_2(A)]}{k_n[N_2(X, v \ge 10)]} = 10^{13}$ cm^{-3} using $[N_2(X, v \ge 10)] = 2 \times 10^{-3}[N_2] \approx 8 \times 10^{13}$ cm^{-3} after [30, 31]. Then, one finds the characteristic frequencies of the previous processes: $\nu_k \approx 1600$ s^{-1}, $\nu_l \approx 120\,000$ s^{-1}, $\nu_m \approx 320$ s^{-1}. The loss of $N_2(A)$, which reads:

$$\begin{aligned}\frac{d[N_2(A)]}{dt} = &-k_k[N_2(A)][N_2(X, 5 \le v \le 14)] - k_l[N_2(A)][N] - k_m[N_2(A)] \\ &+ k_n[N(^2P)][N_2(X, v \ge 10)]\end{aligned} \tag{7}$$

can be written:

$$\frac{d[\mathrm{N_2(A)}]}{dt} \approx -k_l[\mathrm{N_2(A)}][\mathrm{N}] + k_n[\mathrm{N(^2P)}][\mathrm{N_2(X}, v \geq 10)] \tag{8}$$

To integrate this equation, it is essential to know the time dependence of the term $k_n[\mathrm{N(^2P)}][\mathrm{N_2(X}, v \geq 10)]$ otherwise the characteristic frequency of N_2(A) losses would only be set by process (l), which is by far, too high. Consequently, a complete model is required. However, it turns out that the general behaviour of the N_2(A) in late afterglow is satisfactorily described by an exponential decay function [27]:

$$[\mathrm{N_2(A)}] = [\mathrm{N_2(A)}]_0 \exp(-\nu_o t) \tag{9}$$

where ν_o is an overall frequency without physical meaning. This behaviour is strictly followed in our condition as shown in figure 3, in agreement with the previous statement [27]. When the APTES is introduced, the N_2(A) decay shown in figure 3 follows two exponential laws with a change in slope near 25 ms. At shorter times, N_2(A) molecules are likely consumed according to the following process:

$$\mathrm{N_2(A)} + \mathrm{APTES} \rightarrow \mathrm{products} \tag{p}$$

If this process were first-order, the new time evolution of N_2(A) should be:

$$[\mathrm{N_2(A)}] = [\mathrm{N_2(A)}]_0 \exp(-(\nu_o + k_p[\mathrm{APTES}]) \times t) \tag{10}$$

Using data for $t < 25$ ms, one finds $k_p \approx 5.2 \pm 2.0 \times 10^{-15}$ cm^3 s^{-1}, which is about 34 times lower than the rate constant of APTES with N. Here again, the meaning of k_p is debatable, as discussed hereinafter. Nevertheless, the frequencies of processes (j) and (p) defined by reference to the APTES are respectively $\nu_j = k_j$ [N] ~ 500 s^{-1} and $\nu_p = k_p$ [N_2(A)] ~ 0.3 s^{-1}. This shows the negligible role played by N_2(A) on the decomposition of the APTES.

3.3. FTIR spectroscopy

FTIR measurements were performed in the range [500–4000 cm^{-1}] with the Ar–APTES flow, without and with the Ar–N_2 afterglow (Figures 4a to 4c). In table 2, the functional groups in gaseous APTES were identified by comparison of FTIR data with those reported in the literature [32–42].

The absorption band at 785 cm^{-1} (figure 4a) corresponds to NH_2 wagging [34]. This mode has been further confirmed by isotope exchange studies where a red shift of 145 cm^{-1} was observed for the ND_2 wagging mode [34]. This assignment is particularly important because, together with the shoulder at 2745 cm^{-1} (figure 4c) which is attributed by White and Tripp [36] to Si–OH…NH_2, these peaks are the only way to follow the NH_2 group through reaction processes. Indeed, other bands like ν_s (N–H) around 3305 and 3350 cm^{-1} are not detected in our case. The absorption band at 1615 cm^{-1} represents the bending vibration of aliphatic amine (N–H) groups [35] but it is extremely weak and this absorption band cannot be kept to follow the evolution of the NH_2 group in the APTES molecule. It is also true for the band at 3219 cm^{-1} which is due to CH_2–NH_2 [32]. The band at 785 cm^{-1} is higher (typically a tenth of the peak at 1065 cm^{-1}, for instance) and characterized by a broad profile.

The band at 878 cm^{-1} (figure 4a) is due to CH_3 rocking mode [38]. Si–O–C, Si–O in APTES and Si–O–C_2H_5 contribute to bands centred at 1110, 1065 and 958cm^{-1} [33, 34, 36, 38]. CH_2 rocking is observed at 1176 cm^{-1} [37, 38] whereas H–C–H bending is characterized by bands at 1475 and 1449 cm^{-1} [32, 39]. The absorption band at 1241 cm^{-1} corresponds to the asymmetric stretching of SiO–CH_2 [38]. CH_2 bending is observed at 1391 cm^{-1} and corresponds to a CH_2 group distant from Si [34, 35]. Si–O overtones are visible at 2264 and 2116 cm^{-1} [41] (figure 4b). Combinations bands centred at 1938 cm^{-1} are due to Si–O and ρ CH_3 [40]. Vibrations at 2987 cm^{-1}, 2939 cm^{-1}, 2899 cm^{-1} and 2870 cm^{-1} are commonly assigned to symmetric and asymmetric stretching of CH_2 and CH_3 [37, 41]. Finally, the absorption band at 3674 cm^{-1} is assigned to free OH [41], which is likely present because of leakflows, as discussed hereafter.

When the plasma is turned on, new contributions appear (figures 4a, 4b and 4c). Absorption bands at 2140 cm^{-1} and 1733 cm^{-1} are due to CO [38]. H–C vibration in HCN is observed at 3311 cm^{-1} [42]. According to Launer [38], the contribution at 2268 cm^{-1}, simply written CN in table 2, could be assigned either to Si–N=C=O (expected at 2280 cm^{-1}) or to $(RO)_3Si-C_3H_6-C\equiv N$ (expected at 2245 cm^{-1}). There is no amide formation, which would lead to a specific absorption around 1680-1630 cm^{-1}. The contribution at 719 cm^{-1} is due to HCN bending [42]. It is striking that no NH_x contribution appears.

3.4. Mechanisms at stake

The decomposition of APTES might be attributed to N and $N_2(X,v)$ states. To estimate the contribution of the vibrationally-excited nitrogen molecules, a balance on APTES can be done as follows. The consumption rate of APTES through reaction (j) can be written:

$$[\mathrm{APTES}] = [\mathrm{APTES}]_0 \exp\left(-k_j [\mathrm{N}] \times t\right) \tag{10}$$

Using $k_j = 1.8 \pm 0.6 \times 10^{-13}$ cm^3 s^{-1}, one finds that 99% of the precursor should be consumed after ~9.3 ms (or ~5 cm), which is one order of magnitude smaller than N! The reason for this comes from the multiple successive reactions that the APTES can undergo with N atoms without changing drastically its backbone. Each time atomic nitrogen reacts with the APTES molecule to, say, produce a CN radical, the thus-formed fragment of APTES can still react with atomic nitrogen. So, the extra consumption of N atoms in the presence of APTES is not only defined by the APTES molecule but also by all the similar by-products created by the successive reactions with nitrogen atoms. Since the behaviour of N as a function of time follows an exponential decay, this means that N reacts with a molecule which can be considered as almost constant during the first 80 ms. This could be for instance a CH_x group attached to the backbone of the APTES molecule. By using the FTIR contribution at

1241 cm^{-1}, which is characteristic of the APTES backbone, and knowing the concentration of APTES without afterglow (2.1×10^{15} cm^{-3} versus 5.4×10^{13} cm^{-3} in point B – see figure 1 – with the afterglow), it is possible to estimate the concentration of APTES probed by the FTIR beam along its path L. One finds $\overline{[\text{APTES}]}=4.6\times10^{12}$ cm^{-3}. This average value is defined by $\overline{[\text{APTES}]}=\frac{1}{L}\int_0^L[\text{APTES}]_0\exp\left(-\overline{\nu}\frac{x}{v}\right)dx$, where $[\text{APTES}]_0=5.4\times10^{13}$ cm^{-3}. Using L=85 cm, this leads to $\overline{\nu}=81$ s^{-1}, which is lower than the value ν_j = 500 s^{-1} determined by optical emission spectroscopy by a factor of ~6. This discrepancy is clearly due to the successive reactions with N as described previously. Let's consider a new reaction (j):

$$N+\text{"APTES"} \rightarrow \text{products} \qquad \text{(j)}$$

where "APTES" designates the APTES together with its similar by-products. If N reacts with $-CH_2-$ groups of the APTES, then ["APTES"]=6×[APTES]. Consequently, ν_j ~83 $s^{-1}\sim\overline{\nu}$ within the accuracy of the assumptions made. With such a frequency, 99% of the APTES would be consumed only after 58 ms (or 32 cm), which is realistic. The choice of $-CH_2-$ groups, which gives an excellent agreement, is nevertheless illustrative. There is no reason to exclude $-CH_3$ terminal groups for instance, even though their reactivity is likely different. Since we do not know precisely the dissociation mechanisms of the APTES, the previous example is here only to help us describe the role of functional groups on the way nitrogen atoms are consumed.

Then, as nitrogen atoms certainly play a major role in the dissociation of the precursor, the role of the vibrationally-excited states of N_2 is inferred not to be straightforward. Indeed, only sufficiently highly-excited levels might dissociate the APTES but the concentration of levels above v=10 is only a tenth of [N] [30], and so, this process must be limited. Nevertheless, the precise role of $N_2(X,v)$ states is still to be determined.

The fact that N atoms would react preferentially with $–CH_2–$ groups of the APTES, attacking the carbon atoms and not the surrounding hydrogen atoms, is supported by the synthesis of CN bonds within the APTES [38] and HCN groups, as observed by FTIR and OES. No NH_x groups, which could come from the reaction of N or any other active nitrogen species with H atoms of the APTES, are synthesized. NH absorption peaks always decrease in intensity as soon as the discharge is on. No NH emission is observed by optical emission either. Anyway, we notice from FTIR measurements that NH bonds contributions at 785 cm^{-1} and 2745 cm^{-1} becoming very weak but still detectable.

The previous reasoning also applies for $N_2(A)$ and the meaning of k_p is debatable as well. Before 25 ms, a simple quenching of $N_2(A)$ by the APTES could be considered. Beyond 25 ms, $N_2(A)$ certainly reacts with short fragments of APTES, like CO, CN or HCN, the concentration of, say, $–CH_2–$ groups being too weak to still contribute to the loss of $N_2(A)$. In figure 5, the time evolutions of the CH 4300 Å system and the CN violet system as observed by OES are reported. The maximum production of CH excited states is near 20 ms whereas CN radicals have a maximum emission near 35 ms. The existence of these maxima means that these systems are excited stepwise and not straightforwardly. In cold afterglow, the only possible origin of CH* is [43]:

$$C_2 + OH \rightarrow CH^* + CO \qquad \text{(q)}$$

According to Young and Morrow [44], CN is formed from CO in active nitrogen by reaction with an excited state of N_2, probably the $v' = 0$ level of the $W^3\Delta_u$ state, and excited by energy transfer from an excited state of N_2, probably the $^5\Sigma$ state. The $N_2(A)$ state is not involved in either the formation or excitation of CN. The three-body association of C and N to form CN, although important in maintaining a fixed ratio between [C] and [CN], is unimportant. These statements apply only to conditions where [Ar] » [N_2] in the discharge as well as in the observation region and for small additions of CO.

$$CO + N_2\left(W^3\Delta_u\right) \rightarrow CN + NO \tag{r}$$

$$CN + N_2\left({}^5\Sigma\right) \rightarrow CN^* + N_2 \tag{s}$$

The reaction of C_2 with NO to produce CN* would require an excited state of C_2, and this would make the Swan system visible by OES [45].

The synthesis of CN by reaction (r) could also be due to the following processes if the concentration of CO was weak enough [46, 47]:

$$C + N + M \rightarrow CN^* + M \tag{t}$$

$$N + CH \rightarrow CN^* + H \tag{u}$$

Consequently, neither CH nor CN are excited by $N_2(A)$.

The role of impurities (water essentially and, to a lower extent, oxygen from the air, nitrogen being necessarily negligible here) has to be dealt with. Because of the emission of oxygen-containing species without APTES, like the NOβ and NOγ bands, the presence of small leaks is patent. It is worth noting first that no NO groups are present in FTIR spectra without afterglow, which shows that the concentration of NO radicals is much lower than the APTES concentration (6.6×10^{14} cm^{-3}). To quantify these leaks, small amounts of molecular oxygen were introduced on purpose in the afterglow (mixed with the Ar-APTES flow) to determine the influence of impurities, mainly on the $N(^4S)$ time profile. Results (see **supplemental material 3**) show that the time evolution of $N_2(B,v'=11)$ and then, of atomic nitrogen does not change significantly up to 0.15 sccm O_2 ($\sim6\times10^{13}$ cm^{-3}). Meanwhile, the NOβ bands increase in intensity by a factor of 1.7. Then, the concentration of impurities behaving like O_2 is $\sim3\times10^{13}$ cm^{-3}. On the other hand, OH groups at 3674 cm^{-1} are due to impurities. Using a commonly-adopted value of the absorption coefficient for this band (7.3×10^{-19} cm^2) [48, 49], one finds $\left[OH\right]$ $\sim1.1\times10^{15}$ cm^{-3} without afterglow and $\left[OH\right]$ $\sim1.6\times10^{13}$ cm^{-3} with afterglow.

The origin of CO in the FTIR spectra is quite obvious. The oxygen comes undoubtedly from the APTES molecule insofar as increasing the nitrogen flowrate in the discharge induces an increase in CO absorption (figure 6). Here again, using a commonly-adopted value of the absorption coefficient for this band (1.1×10^{-18} cm^2) [49], one finds $[\mathrm{CO}]\sim3.2\times10^{12}$ cm^{-3} in the afterglow. This concentration is about two orders of magnitude lower than the concentration of CO used by Young and Morrow [44] in their experiments. Then, processes (t) and (u) are more likely in the present situation.

3.5. Nanoparticles synthesis

Thin film deposition on the reactor wall is a relatively slow process in the present conditions because of the low partial pressure of the precursor. The deposition rate is about 100 ng mm^{-2} min^{-1}. A thorough description of thin film deposition will be provided in a forthcoming publication. Here, emphasis is placed on the synthesis of nanoparticles in the gas phase. It is important to mention that none of the analyses of the nanoparticles were performed *in situ*. Indeed, after a two-hour treatment, nanoparticles collected on an aluminium substrate were taken out of the experiment and put in contact with the air before being analysed by scanning electron microscopy, transmission electron microscopy and FTIR absorption spectroscopy. In figure 7a, a general view of a typical large sized cluster of agglomerates of nanoparticles is depicted. Agglomerates have diameters of ~200 nm (figure 7b) made of an assembly of amorphous nanoparticles with diameters of a few nanometres (figure 7c).

FTIR analysis of nanoparticles shows, on the contrary, strong changes in absorption bands (figure 8 and table 3). Because of the very high specific area of the collected powders, adsorption of water and CO_2 from the air is important. This can be seen through contributions at 3350 cm^{-1} (due to OH) and 2350 cm^{-1} (due to CO_2). It is known that when aminopropyl compounds are hydrolysed in air, the $-NH_2$ group reacts with carbon dioxide and water and one gets a zwitterionic compound containing $-NH_3^+\ {}^-HCO_3$ groups [38]. However, because the precursor is modified by the plasma treatment, such a structure is not necessarily formed in our conditions. The nanoparticles more likely adopt a salt structure. As shown hereinafter, there is no need to introduce new contributions associated with $–NH_3^+$ and $^-HCO_3$ groups to explain our results. Then, such an interpretation was set aside in favour of a much simpler one, given now. This structure is characterized by the following bands: the broad band between 3650 and 3000 cm^{-1} is attributed to the OH group, the band at 1690 cm^{-1} to the amide I – see **supplemental material 4** for a deconvolution of the bands between 1250 and 1800 cm^{-1}) –, the band at 1575 cm^{-1} (strong – here ~1584) to the amide II and the band at 1480 cm^{-1} (strong – here ~1416) to the C–O–H in plane bending. Then, the doublet band at 658 and 668 cm^{-1} is due to CO_2, likely in carbonate – which would mean that nanoparticles adopt a salt structure after exposure to air – and the band at 719 cm^{-1} to C=O [50]. The oxidation of silicon is also patent thanks to the absorption band at 950 cm^{-1}. This band cannot simply correspond to $Si–O–CH_2–CH_3$ chains because of its high intensity with respect to the Si–O band at 1112 cm^{-1}. The contribution at 808 cm^{-1} is mainly due to Si–O stretching. The ω NH_2 contribution found at 785 cm^{-1} might slightly contribute to this broad peak, but it cannot be the main contributor. XPS results hereinafter will support this assumption. It can be concluded that only a very weak fraction (if any) of the initial content of amine groups in the APTES is retained in the nanoparticles and not undoubtedly observable by FTIR.

At 1260 cm^{-1}, $Si–CH_3$ bonds are likely. A weak contribution at 1730 cm^{-1}, due to ketones, appears as a shoulder of the peak at 1690 cm^{-1} (see **supplemental material 4**). The contribution at 1690 cm^{-1} is certainly due to secondary amides. These amides show an N–H stretching band at 3300–3250 cm^{-1} (here convoluted with the OH band), while the carbonyl stretching (amide I band) is observed at 1680–1640 cm^{-1}. The amide II band for secondary amides is due to the coupling of N–H bending and C–N stretching and appears at 1560–1530 cm^{-1}. A weak band which is an overtone of the amide II band should appear at 3100–3060

cm^{-1}. And a broad N–H wagging band must and does appear at 750–650 cm^{-1}. A weak contribution due to pure ketones is found at 1730 cm^{-1}.

The band at 1690 cm^{-1} cannot be attributed to NH bonds only whose contributions remain weak with respect to Si–O and C–C bonds. Basically, the afterglow treatment is soft and it is expected to retain a higher level of NH_2 groups in the solid than any other process. So roughly, the intensity ratio between Si–O and NH_2 contributions for instance is expected to stay at best the same. Then, if the band at 1690 cm^{-1} were due to NH bonds, the previous ratio would not increase from 0.01 to 1.2.

Auger depth-profile of a single particle (see **supplemental material 5**) gives a N/Si ratio about 0.2. XPS measurements, performed on a set of agglomerates of nanoparticles collected on an aluminium substrate, are depicted in figure 9. Carbon peaks are assigned to C in carbonates CO_3^{2-} (288.7 eV) – which is coherent with the presence of C–O–H vibrations observed by FTIR –, C–O and C–N single bonds (285.5 eV) and C–C or C–H bonds (284.5). Only the Si–O environment is found with a contribution at 102.2 eV. The O1s peak is characterized by 3 components at 533.5, 531.9 and 530.6 eV assigned to O=C (*i.e.* the contribution of the CO_3^{2-} component already observed with carbon), O–H and/or Si–O (*i.e.* the contribution of the Si–O component already observed with silicon) and C–O bonds already observed with carbon. The N1s peak is the sum of two contributions centred at 399.9 eV and 398.4. The first one is clearly due to N–C single bonds in amides (*i.e.* the contribution of the C–N component already observed with carbon) whereas the second one, much lower in intensity (the peak ratio of the correspond areas of these two N contributions is 0.13), might be attributed to N–H in amine, *i.e.* to NH_3^+ in the salt structure. From Auger measurements, we deduce that Si/N(in NH_2) ratio would be 0.026 to be compared with 1 in the APTES molecule. In other words, only a fortieth of the initial NH_2 functional groups would be retained in the nanoparticles. XPS data are consistent with FTIR results.

The Si–O–C structure of the APTES is deeply affected by the treatment and the triplet state of the peak at 1065 cm^{-1} is no longer present. Only two convoluted peaks at 1170 and 1112 cm^{-1} are found. They correspond to LO and TO modes in siloxane groups (Si–O–Si), which explains the loss of oxygen due to the synthesis of CO from the oxygen of the precursor. Silicon binds to another oxygen already attached to a silicon atom. Other minor narrow peaks are also present all over the spectrum but their identification was not possible.

Then, the synthesized nanoparticles are amorphous and show a plasma-polymer like structure where a negligible amount of $–NH_2$ groups is kept. The final composition of the nanoparticles is greatly affected by its contact with the air because of their reactivity with water and CO_2. Then, it is very likely that $–NH_2$ groups are separated from the silicon-containing backbone of the molecule by scission of the C–C bond in the aminopropyl chain of the precursor produced by reaction with N atoms. The formed fragment, non- or weakly reactive is removed by the gas phase and then lacking in the nanoparticles. Most of the nitrogen content found in the nanoparticles comes from the nitrogen atoms of the post-discharge and are present under the form of amides.

CONCLUSION

The interaction of (3–Aminopropyl)triethoxysilane with late Ar-N_2 afterglow is very complex and requires new investigations to be presented more accurately. The following key points were investigated.

- The complete characterization of the Ar-N_2 afterglow in the presence of APTES has been achieved.
- The roles of N and $N_2(A)$ species on the decomposition of APTES have been studied.
- The indexation of the FTIR spectrum of gaseous APTES has been provided.

- The specificity of the synthesis of nanoparticles with regards to the synthesis of thin films has been put forward.
- The composition and the polymeric character of the nanoparticles made from APTES have been clarified.

We could show that nitrogen atoms are likely responsible for the dissociation of the precursor, the vibrationally-excited states of N_2 being able to contribute to this process, but certainly to a lesser degree. $N_2(A)$ states are probably quenched by the APTES and its by-products. The $-NH_2$ group in the precursor is weakly reactive in the afterglow whereas $-CH_x$ groups are directly attacked by N atoms to create CN bonds within the precursor. Emitting CN radicals are produced after several elemental processes via either $C + N + M \rightarrow CN^* + M$ or $N + CH \rightarrow CN^* + H$. CO groups are formed from the oxygen available in the molecule and might leave the silicon atom which creates siloxane bonds. Nanoparticles created in the gas phase show a negligible content of amine groups (about a fortieth of the initial content) and present a non-negligible concentration of nitrogen under the form of secondary amides. They also react with water and CO_2 from the air to produce a salt. Obviously, the method consisting in using a nitrogen afterglow to keep the amine groups is not relevant, although the amine groups are not directly modified by this medium. New strategies are now needed to keep a high retention level of amines in the produced nanoparticles.

ACKNOWLEDGMENTS

This work was done within the framework of the Laboratoire International Associé LIPES, a structure supported by the CNRS to whom we convey our deepest gratitude. We wish to thank also the Région Lorraine and the Institut Carnot ICEEL for the grant of M. GUEYE.

REFERENCES

[1] A. L. Hook, H. Thissen, J. P. Hayes, N. Voelcker, "Smart Materials IV", edited by Nicolas H. Voelcker, Proc. SPIE **2006**, 6413 C1-C11.

[2] H. Li, J. Zhang, X. Zhou, G. Lu, Z. Yin, G. Li, T. Wu, F. Boey, S. S. Venkatraman, H. Zhang, Langmuir **2009**, *26*, 5603

[3] R. G. Acres, A. V. Ellis, J. Alvino, C. E. Lenahan, D. A. Khodakov, G. F. Metha, G. G. Andersson, J. Phys. Chem. C **2012**, *116*, 6289

[4] P. Hamerli, T. Weigel, T. Groth, D. Paul, Biomater. **2003**, *24*, 3989

[5] Ch. Weigel, R. Kellner, Fresenius Z. Anal. Chem. **1989**, *335*, 66

[6] E. T. Vandenberg, L. Bertilsson, B. Liedberg, K. Uvdal, R. Erlandsson, H. Elwing, I. Lundström, J. Colloid Interf. Sci. **1991**, *147*, 103

[7] P. Wikström, C. F. Mandenius, P.-O. Larsson, J. Chromatogr. **1988**, *455*, 105

[8] E. D. Pluddeman, in "Silylated Surfaces" Eds: D. E. Leyden and W. T. Collins, p. 31. Gordon & Breach, New York, **1980**

[9] R. W. Murray, in "Silylated Surfaces" Eds: D. E. Leyden and W. T. Collins, p. 125. Gordon & Breach, New York, **1980**

[10] H. Ishida, Polym. Compos. **1984**, *5*, 101

[11] R. Weissleder, K. Kelly, E. Y. Sun, T. Shtatland, L. Josephson, ().Nature biotechnol. **2005**, *23*, 1418

[12] E. Lecoq, D. Duday, S. Bulou, G. Frache, F. Hilt, R. Maurau, P. Choquet, Plasma Process. Polym. **2013**, *10*, 250

[13] J.N. Borges, T. Belmonte, J. Guillot, D. Duday, M. Moreno-Couranjou, P. Choquet, H.-N. Migeon, Plasma Process. Polym. **2009**, *6*, S490

[14] K. Lachmann, A. Dohse, M. Thomas, C. P. Klages, "Plasma polymerization of 3-aminopropyl-trimethoxysilane inside closed plastic bags at atmospheric pressure",

Proceedings of the 20th International Symposium on Plasma Chemistry (ISPC-20) Philadelphia, Pennsylvania, USA, July 24-29 **2011**

[15] E. R. Beckel, J. M. Slocik, H. Jiang, J. O. Enlow, R. R. Naik, T. J. Bunning, Polymer Preprints, **2005**, *46*, 1269

[16] C. Volcke, R.P. Gandhiraman, V. Gubala, C. Doyle, G. Fonder , P. A. Thiry, A. A. Cafolla, B. James, D.E. Williams, J. Colloid Interface Sci. **2010**, *348*, 322

[17] P. Heyse, M.B. Roeffaers, S. Paulussen, J. Hofkens, P.A. Jacobs, B.F. Sels, Plasma Process. Polym. **2008**, *5*, 186

[18] R.W.B. Pearse, A.G. Gaydon, The identification of molecular spectra, edited by Chapman and Hall, London, **1976**, p. 90

[19] A. Ricard, J. Tétreault, J. Hubert, J. Phys. B: At. Mol. Opt. Phys. **1991**, *24*, 1115

[20] A. Ricard, S.-G. Oh, V. Guerra, Plasma Sources Sci. Technol. **2013**, *22*, 035009

[21] G. Callede, J. Deschamps, J. L. Godart, A. Ricard, J. Phys. D: Appl. Phys. **1991**, *24*, 909

[22] L.G. Piper, J. Chem. Phys. **1992**, *97*, 270

[23] R. L. Brown, J. Chem. Phys. **1970**, *52*, 4604

[24] D. W. Setser, D. H. Stedman, J. A. Coxon, J. Chem. Phys. **1970**, *53*, 1004

[25] S. S. Sulakshin, Soviet Phys. J. **1980**, *23*, 991

[26] I. A. Kossyi, A. Yu. Kostinsky, A. A. Matveyev, V. P. Silakov, Plasma Sources Sci. Technol. **1992**, *1*, 207

[27] N. Sadeghi, C. Foissac, P. Supiot, J. Phys. D: Appl. Phys. **2001**, *34*, 1779

[28] J. Henriques, E. Tatarova, V. Guerra, C. M. Ferreira, J. Appl. Phys. **2002**, *91*, 5622

[29] L. G. Piper, J. Chem. Phys. **1989**, *91*, 864

[30] P. A. Sá, J. Loureiro, J. Phys. D: Appl. Phys. **1997**, *30*, 2320

[31] V. Guerra, P. A. Sá, J. Loureiro, Eur. Phys. J. Appl. Phys. **2004**, *28*, 125

[32] Ch. Weigel, R. Kellner, Fresenius Z. Anal. Chem. **1989**, *335*, 663

[33] E. Finocchio, E. Macis, R. Raiteri, G. Busca, Langmuir **2007**, *23*, 2505

[34] V. R. Rai, S. Agarwal, Chem. Mater. **2011**, *23*, 2312

[35] I.A. Rahman, M. Jafarzadeh, C.S. Sipaut, Ceram. Int., **2009**, *35*, 1883

[36] L. D. White, C. P. Tripp, J. Colloid Interf. Sci. **2000**, *232*, 400

[37] N. Aissaoui, L. Bergaoui, J. Landoulsi, J.-F. Lambert, S. Boujday, Langmuir **2012**, *28*, 656

[38] P. J. Launer, "Infrared analysis of organosilicon compounds: spectra-structure correlations", Silicone compounds register and review **1987**, 100

[39] H. Okabayashi, I. Shimizu, E. Nishio, C. J. O'Connor, Colloid Polym. Sci. **1997**, *275*, 744

[40] Jr J.Workman, L. Weyer, "Practical guide to interpretive near-infrared spectroscopy", edited by CRC press, **2007**

[41] J. Coates, "Interpretation of infrared spectra, a practical approach", Encyclopedia of analytical chemistry, edited by John Wiley & Sons Ltd, Chichester, **2000**

[42] P. Linstrom, W.G. Mallard, "NIST Chemistry WebBook" NIST Standard Reference Database Number 69, National Institute of Standards and Technology: Gaithersburg, MD, June 2005; HCN. http://webbook.nist.gov (accessed on Apr. 02, 2015).

[43] Y. Hidaka, Bull. Chem. Soc. Jap. **1982**, *55*, 351

[44] R. A. Young, W. Morrow, J. Chem. Phys. **1974**, *60*, 1005

[45] H. Reisler, J. Chem. Phys. **1980**, *73*, 2280

[46] G Dilecce, P F Ambrico, M Simek, S De Benedictis, J. Phys.: Conf. Series **2010**, *227*, 012003

[47] I.W.M Smith, Int. J. Mass spec. ion. Phys. **1995**, *149*, 231

[48] J. Mathias, G. Wannemacher, J. Coll Interf. Sci. **1988**, *125*, 61

[49] M.E. Palumbo, G. Strazzulla, Astron. Astrophys. **1993**, *269*, 568

[50] X. Jia, Q. Zhang, M.-Q. Zhao, G.-H. Xu, J.-Q. Huang, W. Qian, Y. Lu, F. Wei, J. Mater. Chem. **2012**, *22*, 7050

FIGURE CAPTION

Figure 1: The experimental setup.

Figure 2: Optical emission spectra of Ar-N_2 afterglow with and without APTES.

Figure 3: Time evolution of N(^{4}S) and N_2(A) states with and without APTES.

Figure 4: Gas phase FTIR spectra of the Ar-APTES flow without (red) and with (black) the Ar-N_2 afterglow. Infrared region: a) from 1700 to 500 cm^{-1}, b) from 2600 to 1700 cm^{-1} and c) from 4000 to 2600 cm^{-1}. Resolution: 2 cm^{-1}.

Figure 5: Time evolution of the CH 4300 Å system and the CN violet system.

Figure 6: Influence of the nitrogen flow rate on the absorbance of specific FTIR bands.

Figure 7: a) SEM image of nanoparticles collected on an aluminium substrate. b) TEM image of a micrometric cluster made of agglomerates with mean sizes of about 200 nm. Dotted lines show the boundaries between selected agglomerates. c) TEM image at high magnification showing amorphous elemental nanoparticles.

Figure 8: FTIR spectrum of solid nanoparticles collected in the gas phase. Infrared region: from 4000 to 600 cm^{-1}. Resolution: 2 cm^{-1}.

Figure 9: C1s, N1s, Si2p and O1s XPS spectra of a set of nanoparticles collected on an aluminium substrate.

Table 1: List of all the transitions observed in afterglow.

Table 2: Vibrational groups and their corresponding frequencies observed in Ar-N_2 afterglow with (bold) and without APTES.

Table 3: Main vibrational groups and their corresponding frequencies observed in nanoparticles produced from APTES. vw: very weak. sh.: shoulder.

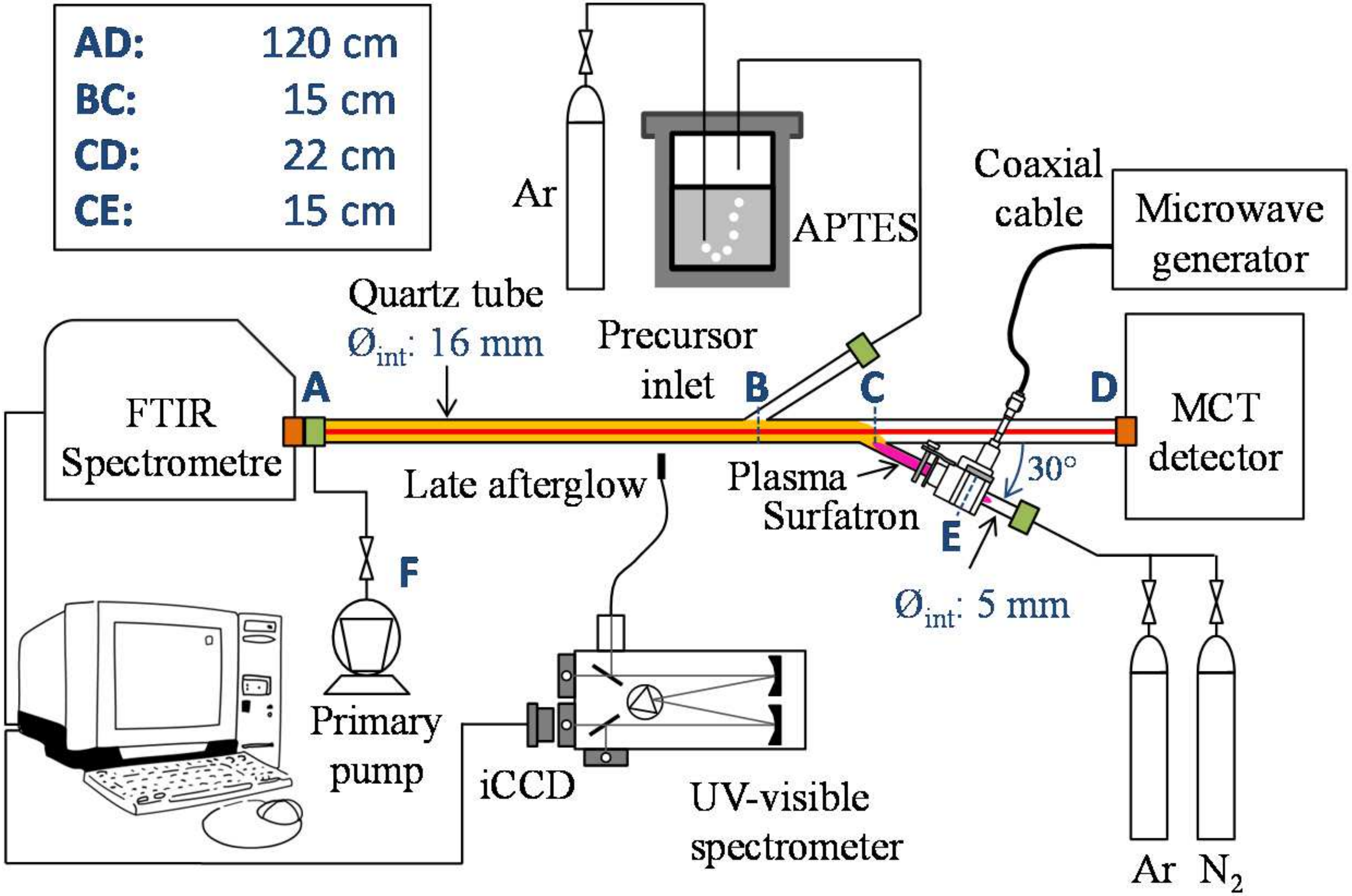

Figure 1: The experimental setup.

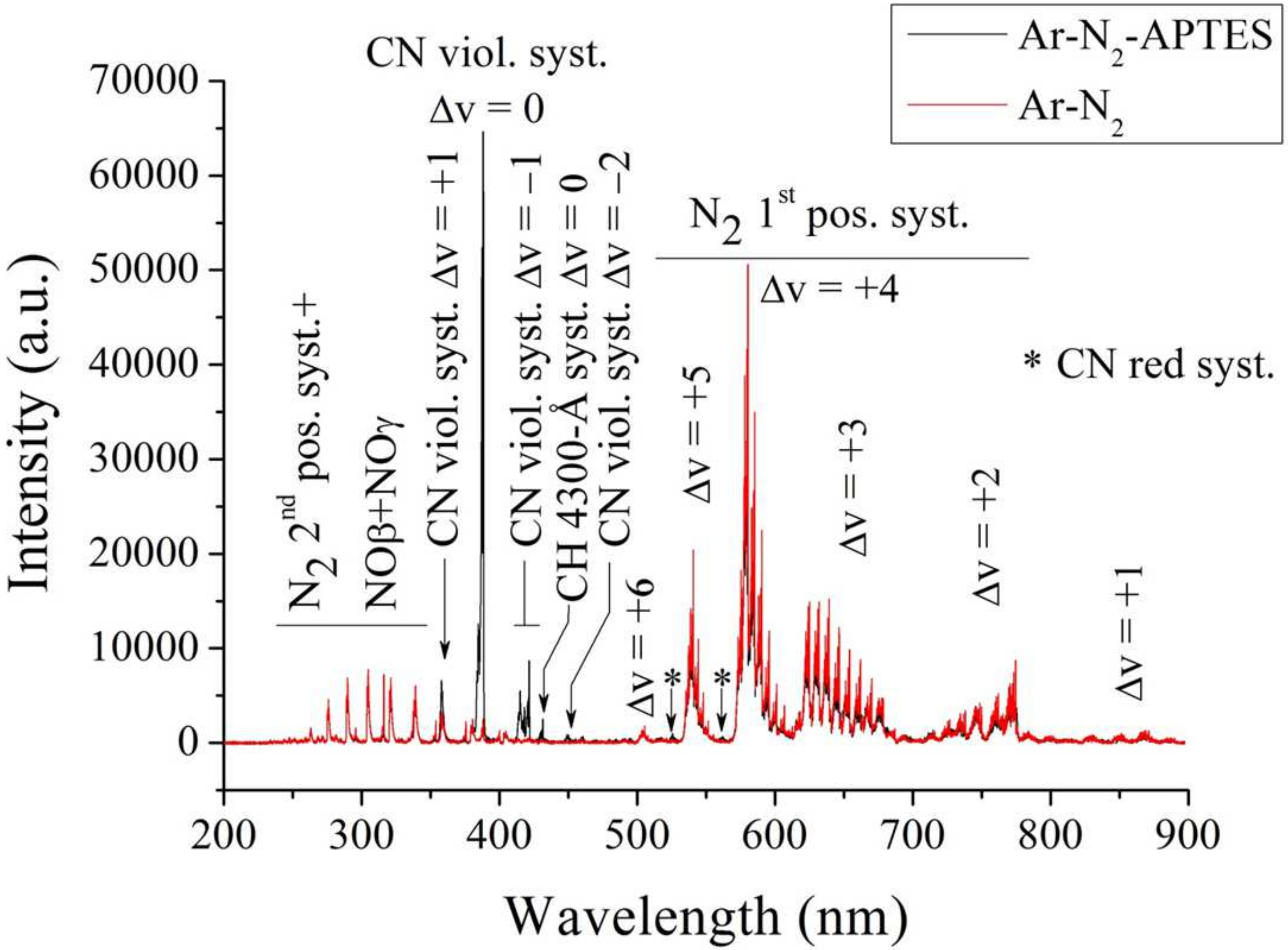

Figure 2: Optical emission spectra of Ar-N_2 afterglow with and without APTES.

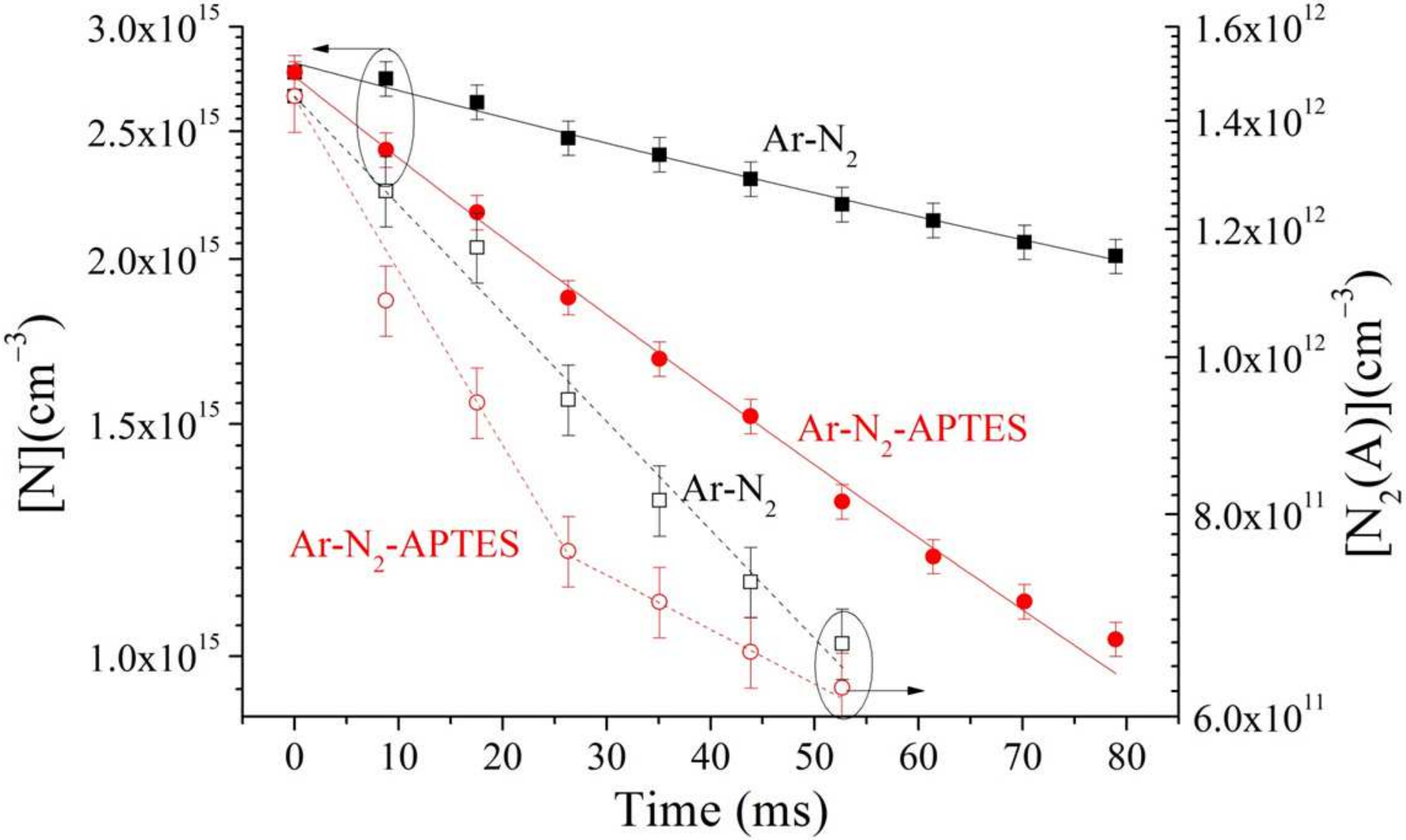

Figure 3: Time evolution of N(^{4}S) and N_2(A) states with and without APTES.

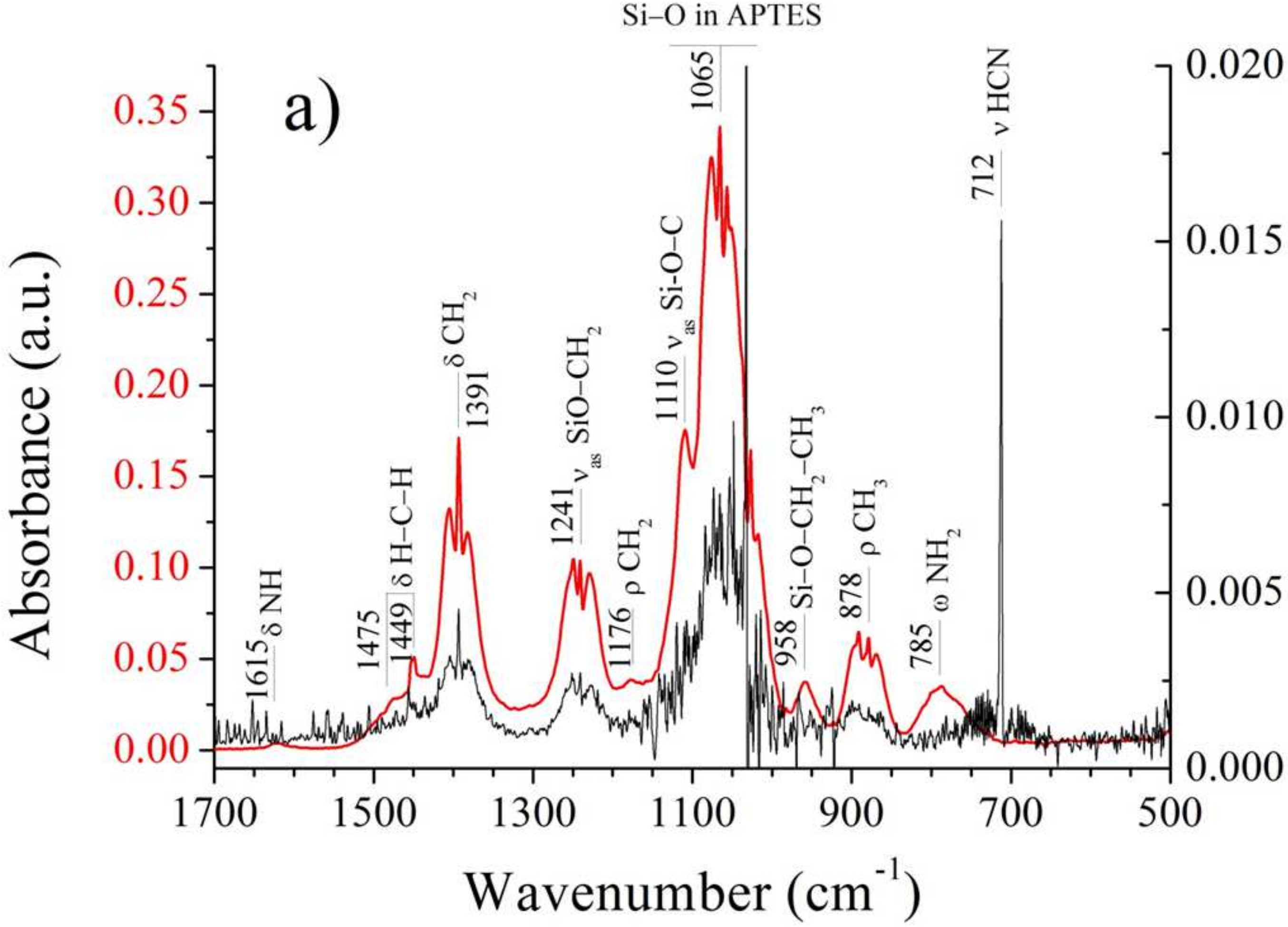

Figure 4a: Gas phase FTIR spectra of the Ar-APTES flow without (red) and with (black) the Ar-N_2 afterglow. Infrared region: from 1700 to 500 cm^{-1}. Resolution: 2 cm^{-1}.

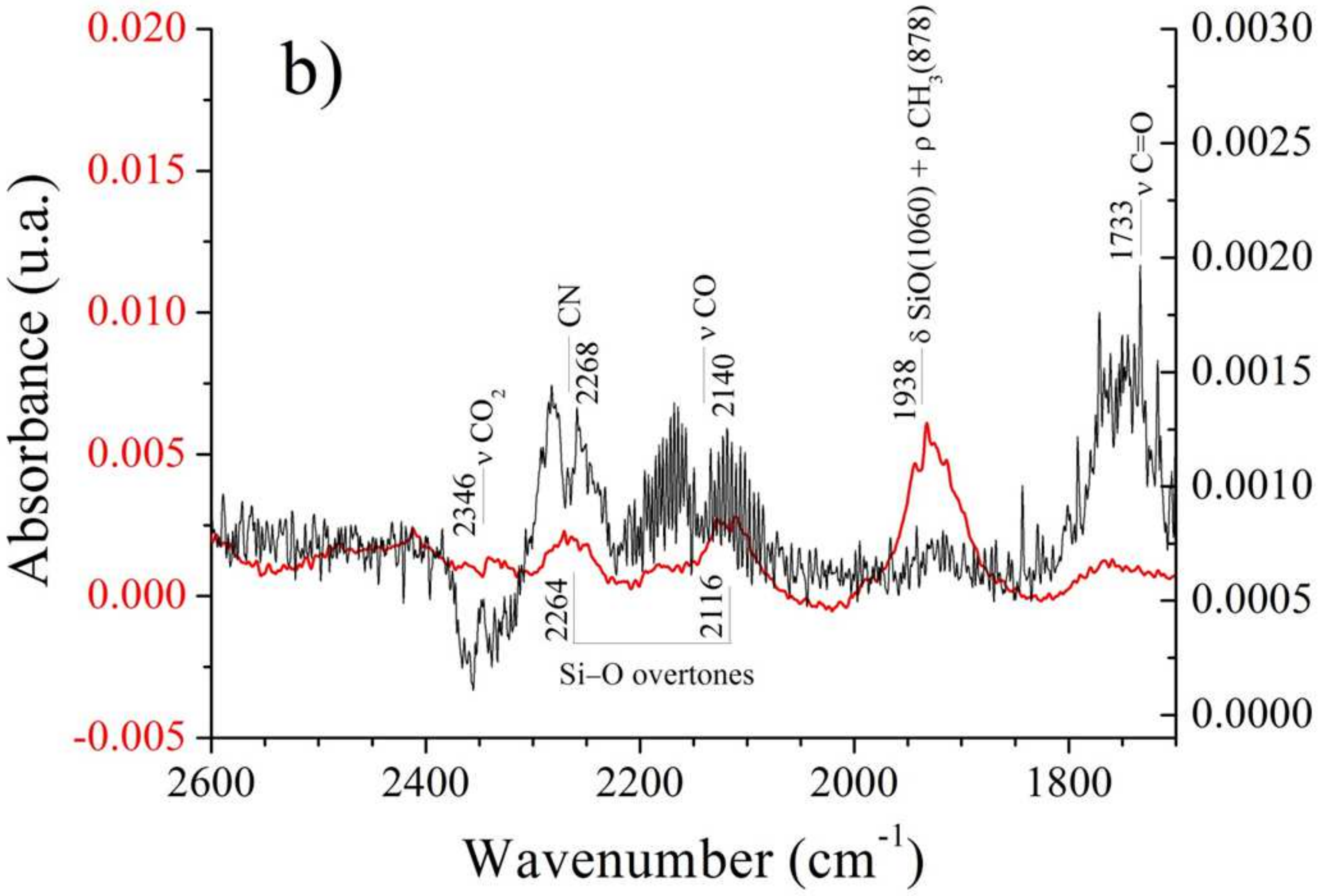

Figure 4b: Gas phase FTIR spectra of the Ar-APTES flow without (red) and with (black) the Ar-N_2 afterglow. Infrared region: from 2600 to 1700 cm^{-1}. Resolution: 2 cm^{-1}.

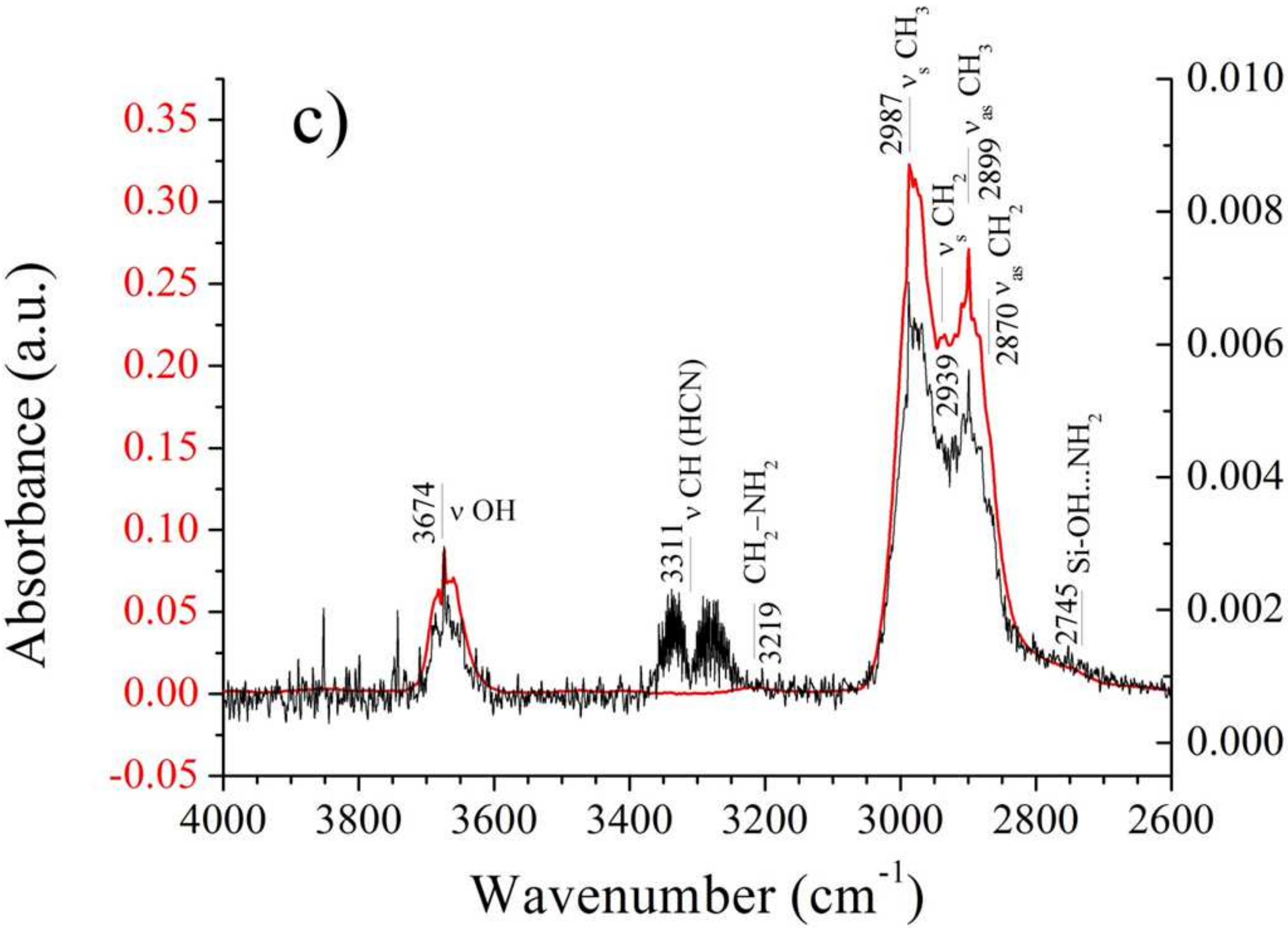

Figure 4c: Gas phase FTIR spectra of the Ar-APTES flow without (red) and with (black) the Ar-N_2 afterglow. Infrared region: from 4000 to 2600 cm^{-1}. Resolution: 2 cm^{-1}.

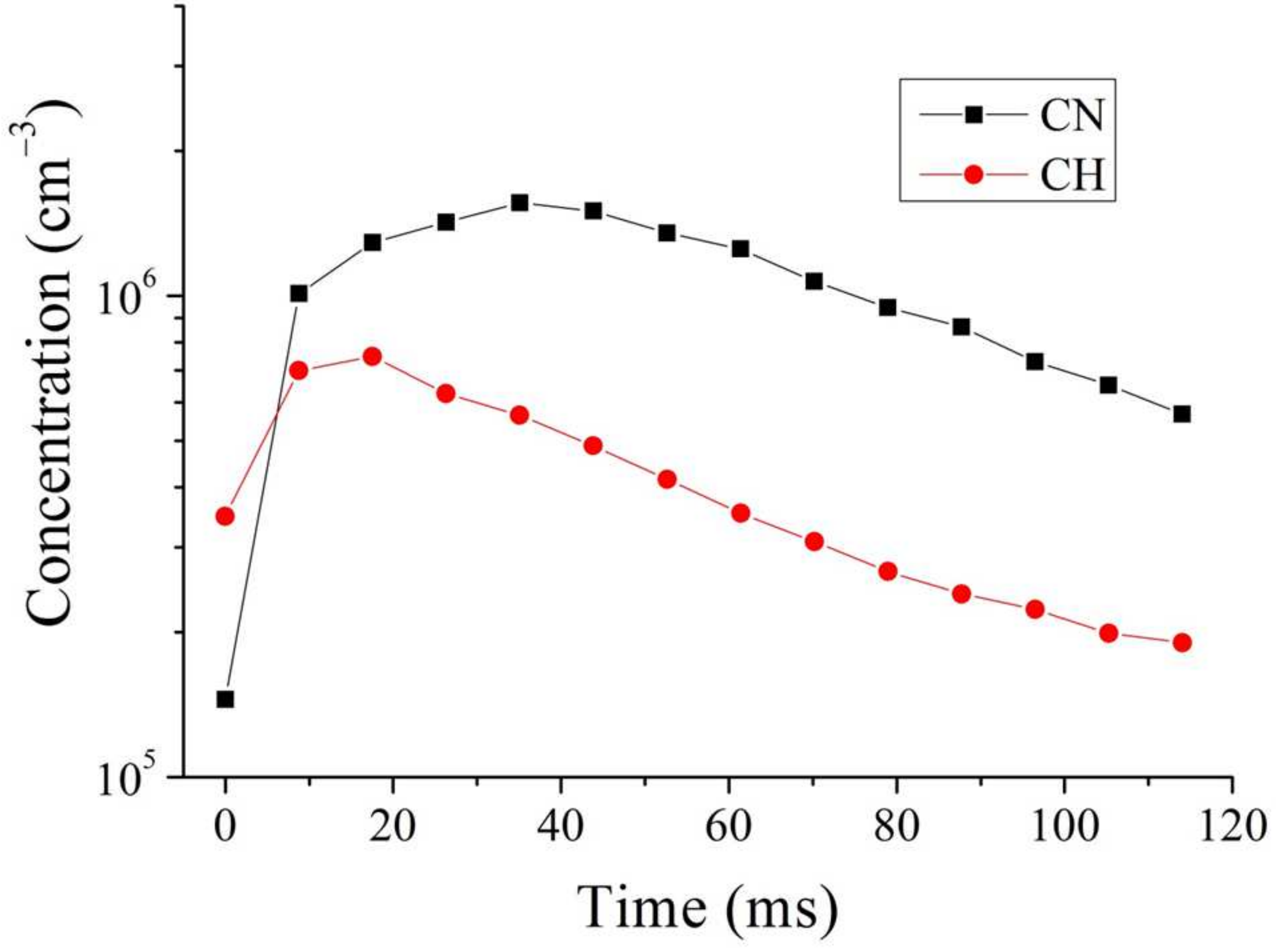

Figure 5: Time evolution of the CH 4300 Å system and the CN violet system.

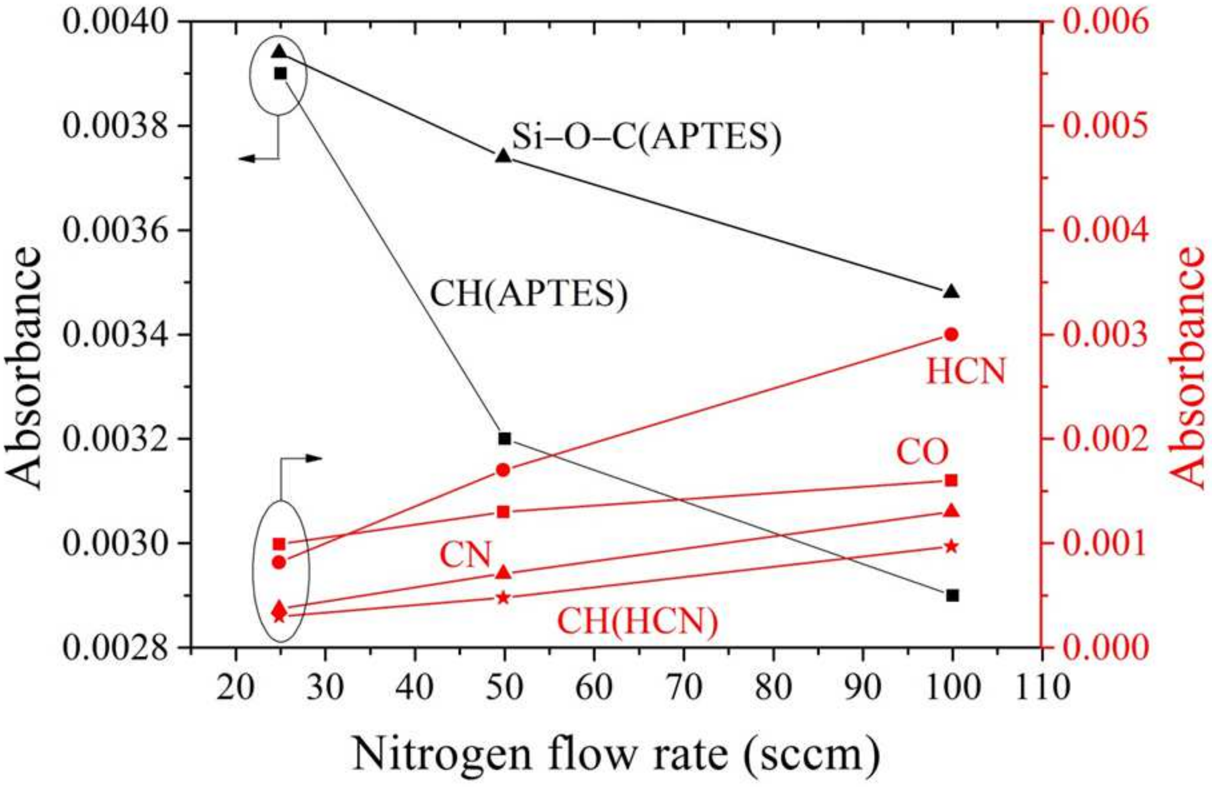

Figure 6: Influence of the nitrogen flow rate on the absorbance of specific FTIR bands.

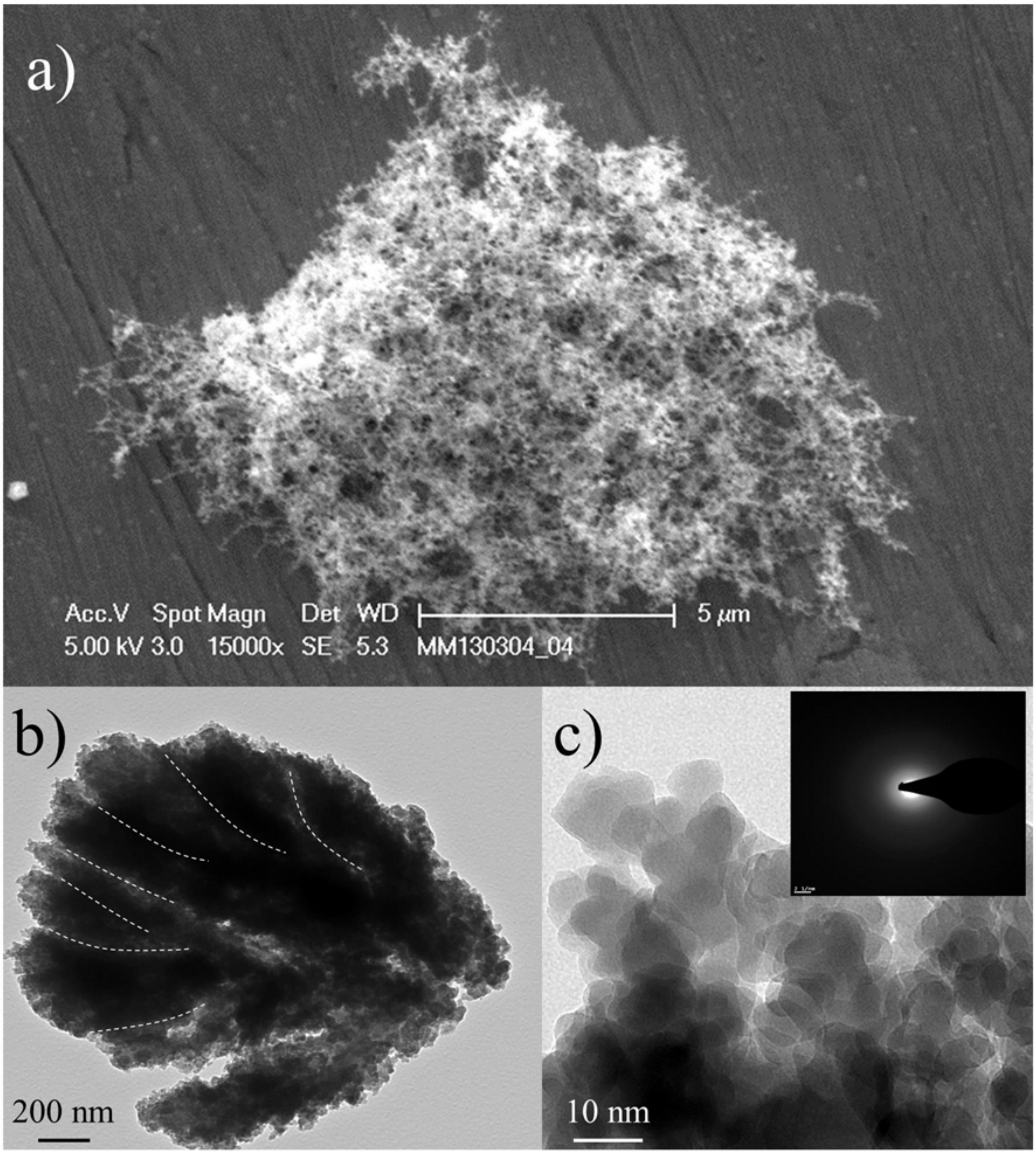

Figure 7: a) SEM image of nanoparticles collected on an aluminium substrate. b) TEM image of a micrometric cluster made of agglomerates with mean sizes of about 200 nm. Dotted lines show the boundaries between selected agglomerates. c) TEM image at high magnification showing amorphous elemental nanoparticles.

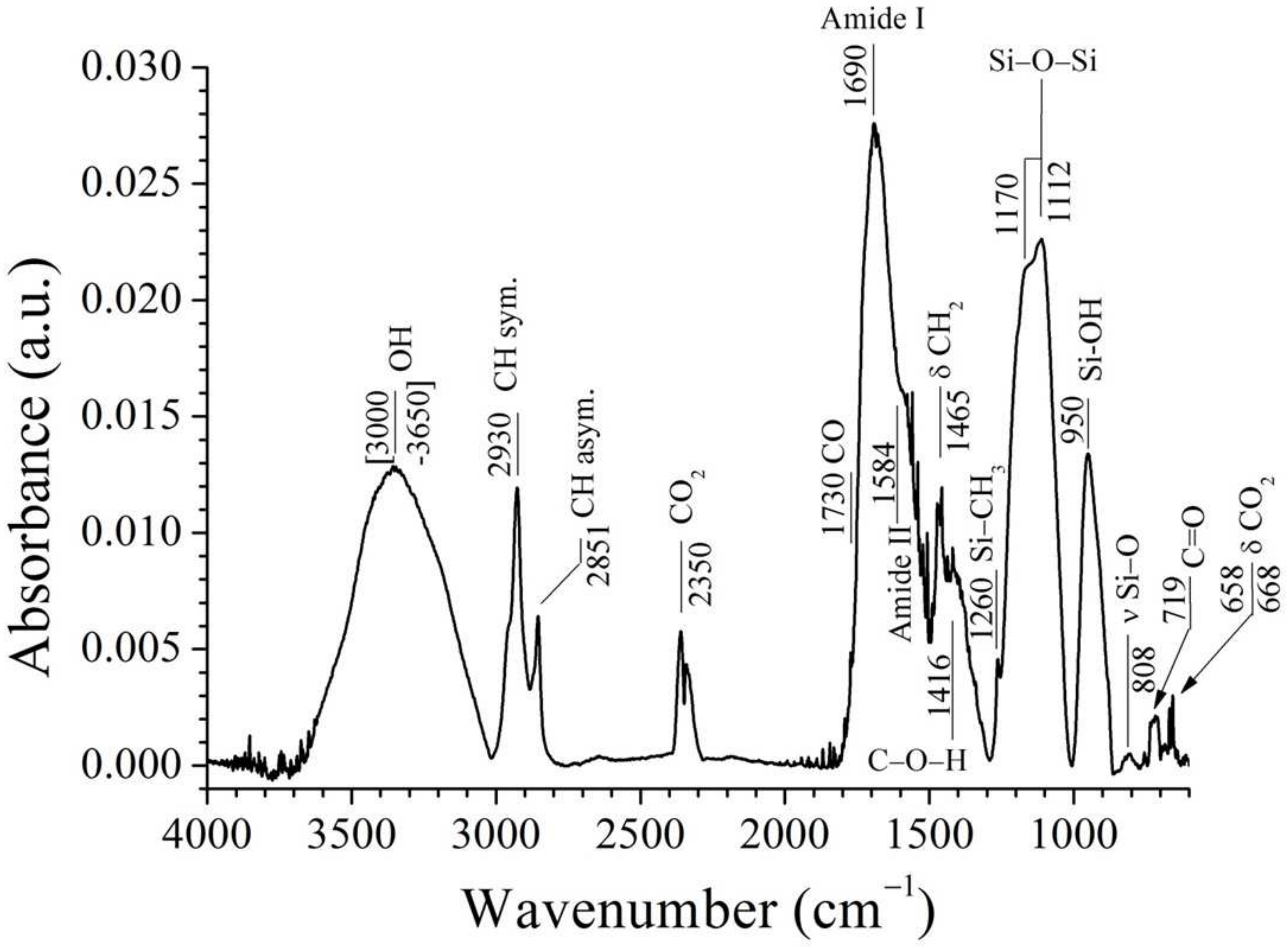

Figure 8: FTIR spectrum of solid nanoparticles collected in the gas phase. Infrared region: from 4000 to 600 cm^{-1}. Resolution: 2 cm^{-1}.

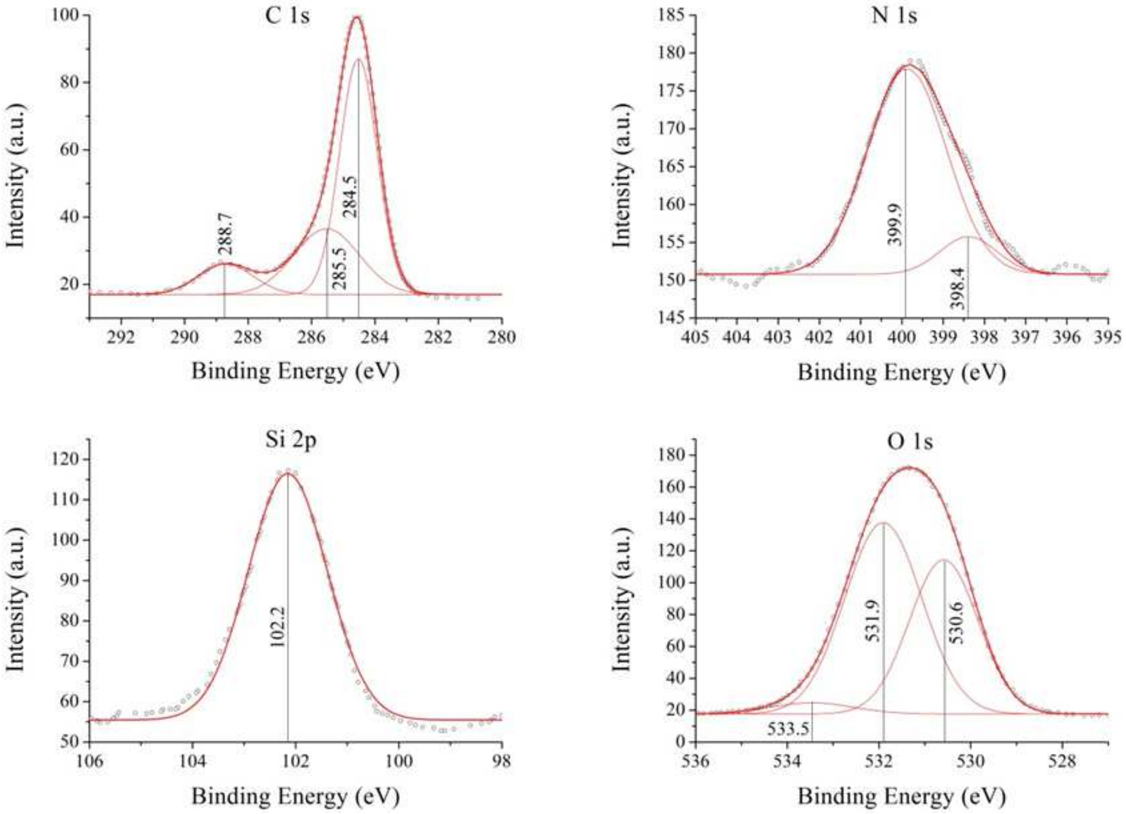

Figure 9: C1s, N1s, Si2p and O1s XPS spectra of a set of nanoparticles collected on an aluminium substrate.

Condition	Species	Transition	System name	Intensity	Δv
w/ or w/o APTES	N_2	$N_2\ (B^3\Pi_g, v' \rightarrow A^3\Sigma_u^+, v'')$	first positive system	Strong	from +6 to +1
	N_2	$N_2\ (C^3\Pi_u, v' \rightarrow B^3\Pi_g, v'')$	second positive system	Moderate	from −1 to +4
	NO	$NO\ (B^2\Pi, v' \rightarrow X^2\Pi, v'')$	NOβ	Moderate	from +13 to +3
	NO	$NO\ (A^2\Sigma^+, v' \rightarrow X^2\Pi, v'')$	NOγ	Weak	from +2 to +5
w/ APTES only	CN	$CN\ (B^2\Sigma^+, v' \rightarrow X^2\Sigma^+, v'')$	CN violet	Strong	$\Delta v = -1, 0, +1$
	CN	$CN\ (A^2\Pi, v' \rightarrow X^2\Sigma^+, v'')$	CN red	Weak	from −3 to −6
	CH	$CH\ (A^2\Delta_g, v' \rightarrow X^2\Pi_u, v'')$	CH 4300Å	Moderate	$\Delta v = 0$

Table 1: List of all the transitions observed in afterglow.

Assignments	Frequency	Ref.	Assignments	Frequency	Ref.	Assignments	Frequency	Ref.
ν OH	3674 cm^{-1}	[41]	**CN**	**2268 cm^{-1}**	[38]	ν_{as} SiO–CH_2	1241 cm^{-1}	[38]
ν CH (HCN)	**3311 cm^{-1}**	[42]	**ν CO**	**2140 cm^{-1}**	[38]	ρ CH_2	1176 cm^{-1}	[37, 38]
CH_2–NH_2	3219 cm^{-1}	[38]	Si–O overtones	2116 & 2264 cm^{-1}	[41]	ν_{as} Si–O–C	1110 cm^{-1}	[36]
ν_s CH_3	2987 cm^{-1}	[41]	Si–O + ρ CH_3	1938 cm^{-1}	[40]	Si–O in APTES	1065 cm^{-1}	[33, 34, 38]
ν_s CH_2	2939 cm^{-1}	[37, 41]	**ν C=O**	**1733 cm^{-1}**	[38]	Si–O–C_2H_5	958 cm^{-1}	[38]
ν_{as} CH_3	2899 cm^{-1}	[41]	δ NH	1615 cm^{-1}	[35]	ω NH_2	785 cm^{-1}	[34]
ν_{as} CH_2	2870 cm^{-1}	[37, 41]	δ H–C–H	1449 & 1475 cm^{-1}	[32, 39]	ρ CH_3	878 cm^{-1}	[38]
Si–OH…NH_2	2745 cm^{-1}	[36]	δ CH_2 (distant from Si)	1391 cm^{-1}	[34,35]	**ν HCN**	**712 cm^{-1}**	[42]

Table 2: Vibrational groups and their corresponding frequencies observed in Ar-N_2 afterglow with (bold) and without APTES.

Assignment	Comment	Frequency	Ref.	Assignment	Comment	Frequency	Ref.
δ CO_2	doublet	668 & 658 cm^{-1}	[38]	δ CH_2	triplet	1465 cm^{-1}	[38]
C=O	broad	719 cm^{-1}	[50]	Amide II	strong	1584 cm^{-1}	[38]
ν Si–O	broad	808 cm^{-1}	[34]	Amide I	strong	1690cm^{-1}	
Si–OH		950 cm^{-1}	[38]	C=O	weak – sh.	1730 cm^{-1}	[8]
ν_{as} Si–O–Si	LO mode	1170 cm^{-1}	[36-38]	CO_2	doublet	2350 cm^{-1}	
ν_{as} Si–O–Si	TO mode	1096 cm^{-1}	[36-38]	ν_{as} CH_3		2851 cm^{-1}	[41]
Si–CH_3	vw	1260 cm^{-1}	[38]	ν_s CH_3		2930 cm^{-1}	[41]
C-O-H	strong	1416 cm^{-1}	[32,39]	ν OH	very broad	3000-3650 cm^{-1}	[41]

Table 3: Main vibrational groups and their corresponding frequencies observed in nanoparticles produced from APTES. vw: very weak. sh.: shoulder.

SUPPLEMENTAL MATERIALS

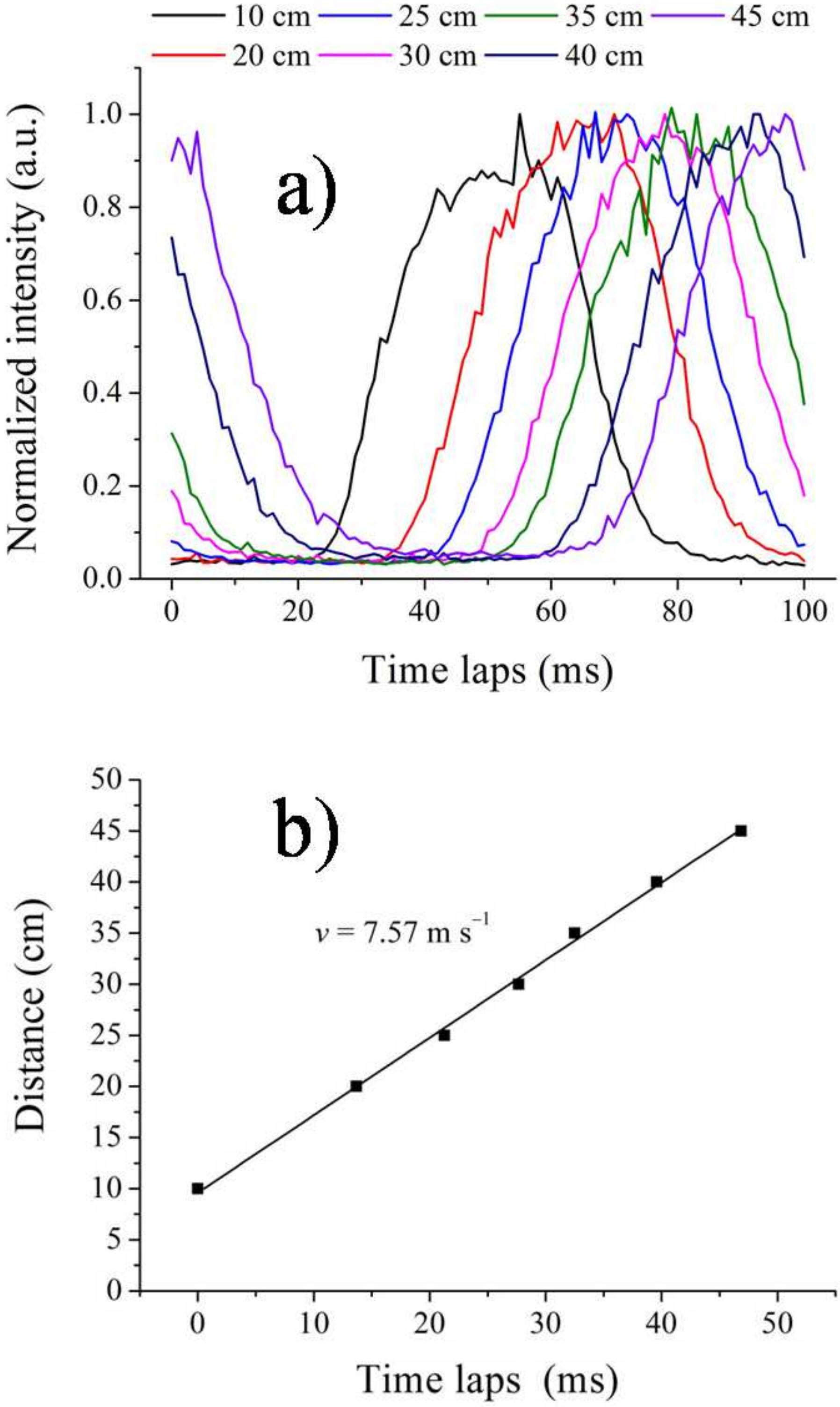

Supplemental material 1: a) Time-resolved emission of the N_2 ($B^3\Pi_g$, $v'=11 \rightarrow A^3\Sigma_u^+$, $v''=7$) transition at 580.43 nm observed for different distances to point B (see figure 1). The plasma is pulsed at 10 Hz and the duty cycle is 60%. b) Distance to point B as a function of the time laps giving the gas velocity in the afterglow tube.

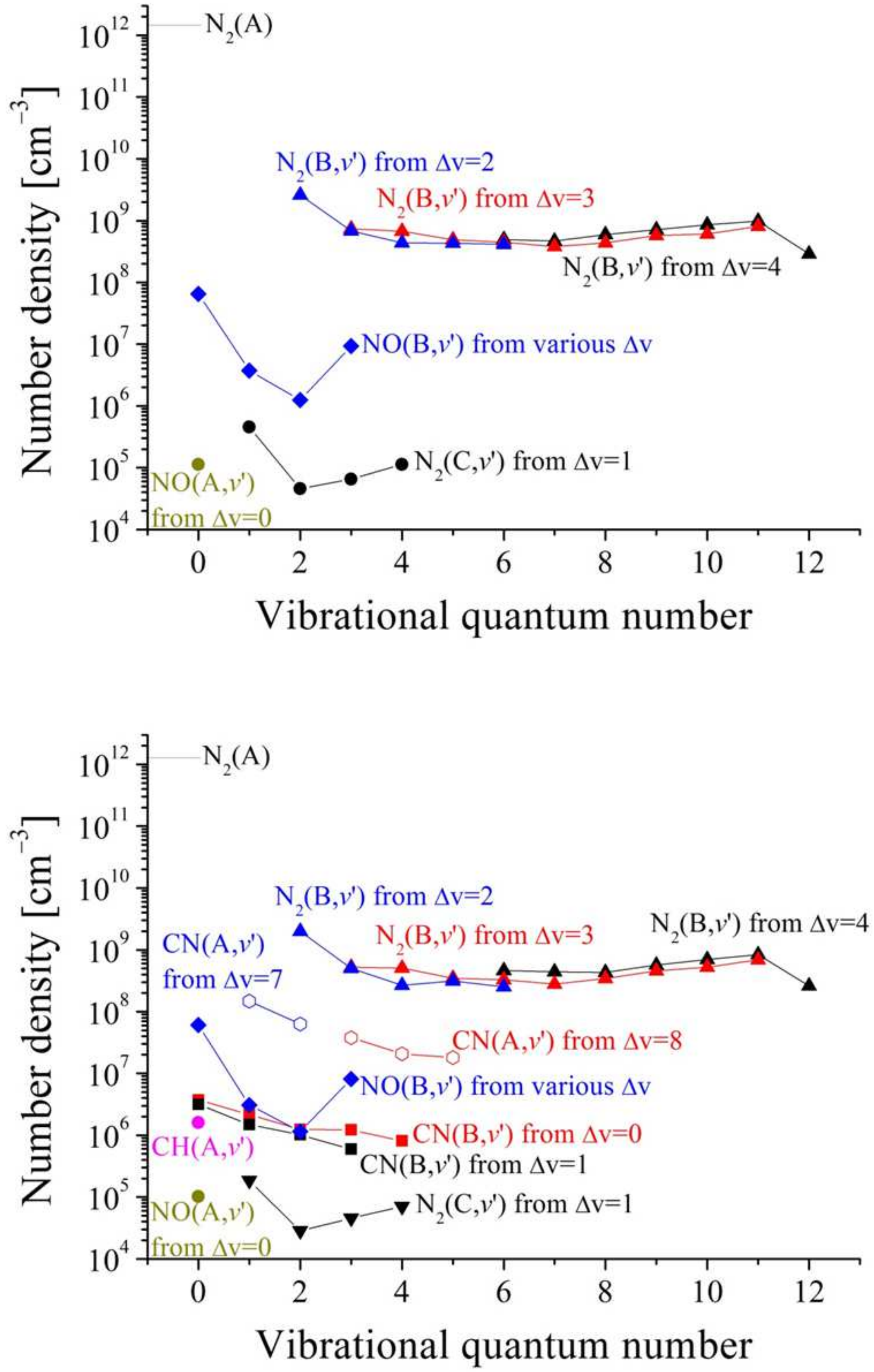

Supplemental material 2: Species number density a) without APTES b) with APTES.

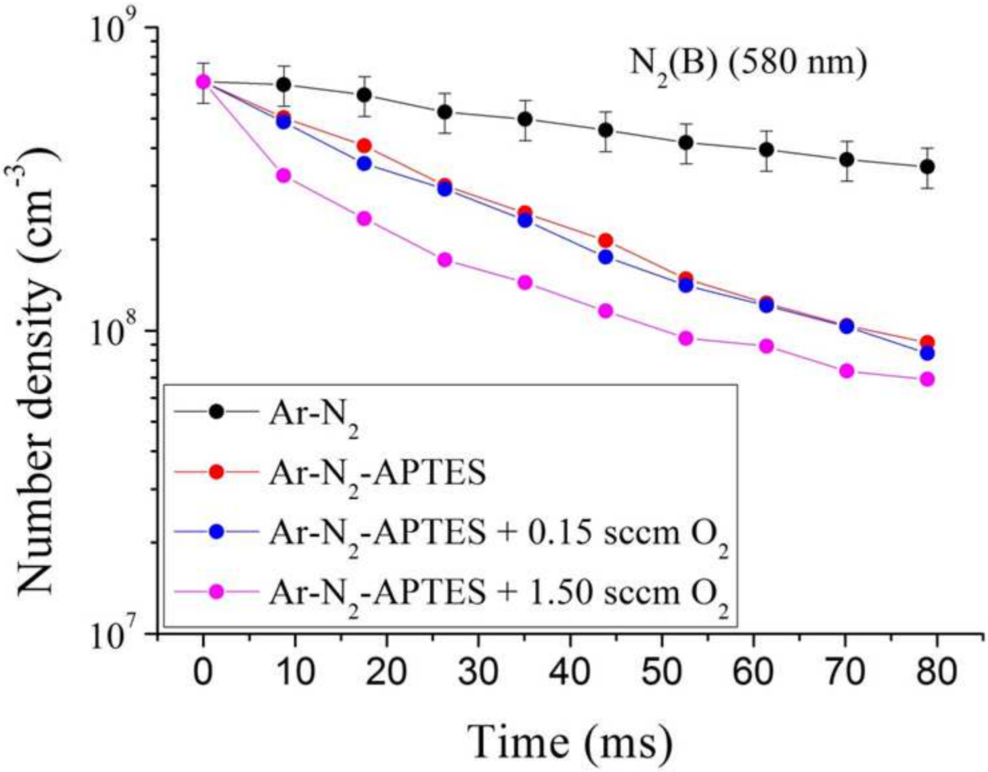

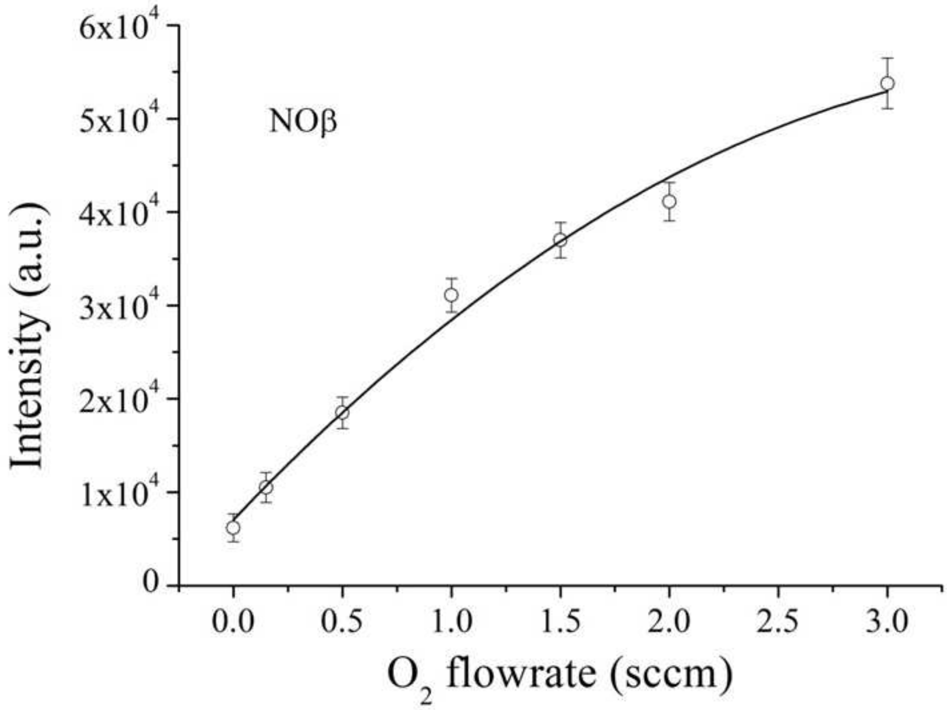

Supplemental material 3: a) Time evolution of the species number density of $N_2(B,v'=11)$ and b) evolution of NOβ OES intensity for different oxygen flowrate in afterglow.

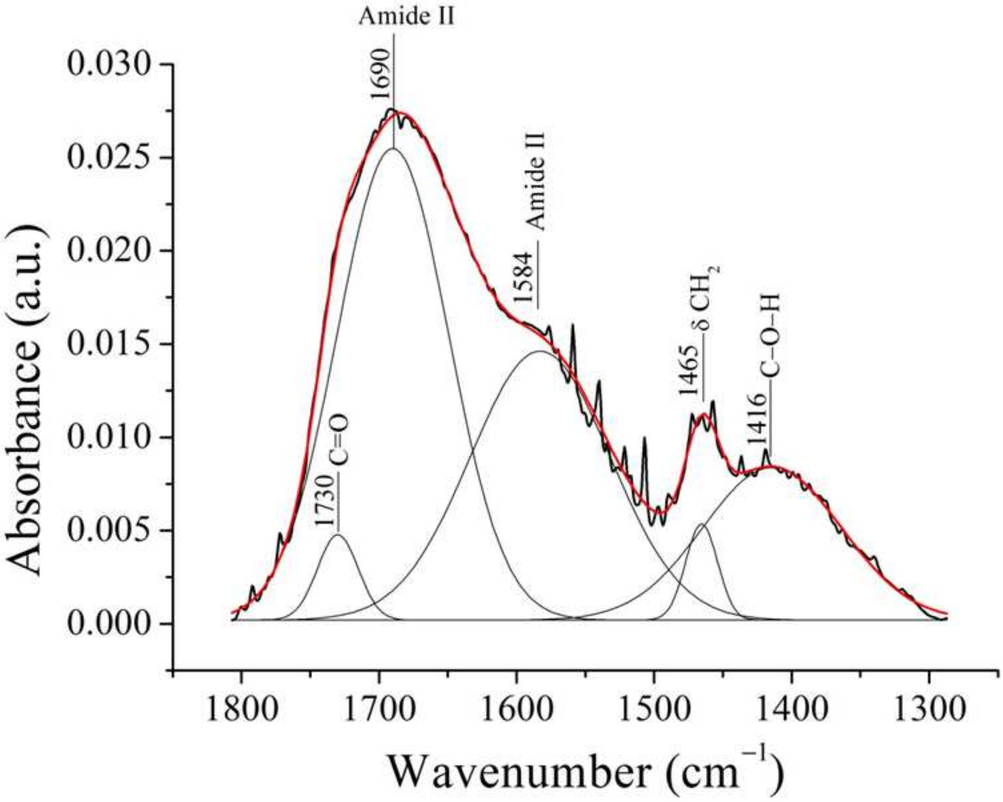

Supplemental material 4: Deconvolution with Gaussian profiles of the bands between 1800 and 1250 cm^{-1}.

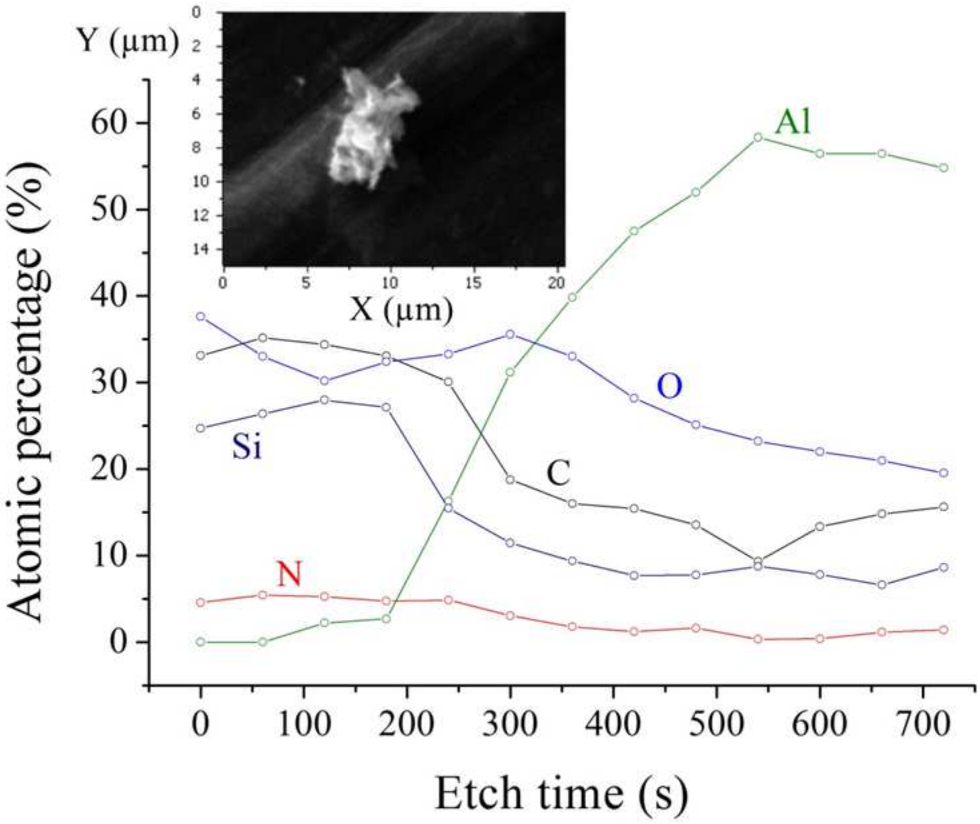

Supplemental material 5: Depth-profiles on a single agglomerate obtained by Auger from C KL_1, N KL_1, O KL_1, Al KL_1 and Si KL_1 transitions. The SEM image of the corresponding agglomerate is shown in insert. The mean composition of the agglomerate, determined from the signals measured over the depth where the Al intensity is null, i.e. where the substrate is not probed, is Si: ~25 at.%, O: ~35 at.%, N: ~5 at.% and C: ~35 at.%.